

Max-Planck-Institut  
für Astrophysik



Technische Universität München  
Fakultät für Physik

Abschlussarbeit im Masterstudiengang  
Kern-, Teilchen- und Astrophysik

# Stellar Collapse Diversity and the Diffuse Supernova Neutrino Background

Daniel Kresse

23. November 2018

Erstgutachter (Themensteller): Apl. Prof. Dr. Hans-Thomas Janka  
Zweitgutachter: Prof. Dr. Lothar Oberauer



# Contents

<b>1. Introduction</b>	<b>1</b>
<b>2. Simulation Setup and Neutrino Signals</b>	<b>5</b>
2.1. Pre-Supernova Models . . . . .	5
2.2. Supernova Simulations . . . . .	5
2.3. Neutrino Signals . . . . .	7
<b>3. Formulation of the DSNB</b>	<b>11</b>
3.1. Time-Integrated Neutrino Spectra . . . . .	11
3.2. IMF-Weighted Average . . . . .	12
3.3. Cosmic Core-Collapse Rate . . . . .	13
3.4. Cosmological Model . . . . .	13
3.5. Low-Mass NS-Formation Events . . . . .	14
<b>4. DSNB Parameter Study</b>	<b>15</b>
4.1. DSNB Components . . . . .	15
4.2. DSNB Parameter Dependence . . . . .	17
4.3. Additional Low-Mass Component . . . . .	20
4.4. Most Extreme Cases and Comparison with the SK-Flux Limits . . . . .	22
<b>5. Fiducial DSNB Predictions and Remaining Uncertainties</b>	<b>25</b>
5.1. Fiducial Parameter Choices . . . . .	25
5.2. Neutrino Flavor Conversions . . . . .	26
5.3. Remaining Uncertainties . . . . .	29
5.4. Comparison with Previous Works . . . . .	30
<b>6. Summary and Conclusions</b>	<b>31</b>
<b>A. Extrapolation of neutrino signals</b>	<b>33</b>
<b>B. Flavor rescaling</b>	<b>37</b>
<b>C. Total energies of radiated neutrinos</b>	<b>41</b>
<b>D. Spectral Shapes</b>	<b>45</b>
<b>E. List of Abbreviations</b>	<b>49</b>
<b>Bibliography</b>	<b>53</b>



# Chapter 1.

## Introduction

When a massive star (above  $\sim 9M_{\odot}$ ) ends its life with the collapse of the inner core to a neutron star (NS) or a black hole (BH), a tremendous amount of gravitational binding energy (several  $10^{53}$  erg) is released, predominantly in the form of neutrinos and antineutrinos (see, e.g., Janka, 2012, 2017; Burrows, 2013). In 1987, when the blue supergiant Sanduleak -69° 202 (Walborn et al., 1987) in the Large Magellanic Cloud exploded as supernova (SN) 1987A, such an associated neutrino burst was detected for the first (and so far only) time as a  $\sim 10$  s long signal, however, with the sparse yield of only two dozen counts (Hirata et al., 1987; Bionta et al., 1987; Alexeyev et al., 1988). Nowadays, neutrino observatories all over the world have advanced significantly such that a galactic SN would lead to a high-statistics signal (e.g., Ikeda et al., 2007; Abbasi et al., 2011), which the scientific community is eagerly waiting for.

While such a nearby SN is a rare event (Diehl et al., 2006; Ikeda et al., 2007; Agafonova et al., 2015), a vast number of massive stars already ended their lives in the cosmic history, generously radiating neutrinos. The integral flux from all those past core collapses at cosmological distances, which is steadily flooding Earth, constitutes the so-called diffuse supernova neutrino background (DSNB). It makes for a “guaranteed” (isotropic and stationary) signal of MeV neutrinos, comprising rich information on the entire population of stellar core collapses (for dedicated reviews, see Ando & Sato, 2004; Beacom, 2010; Lunardini, 2016). Intriguingly, the Super-Kamiokande (SK) experiment set upper flux limits on the DSNB (Malek et al., 2003; Bays et al., 2012; Zhang et al., 2015) which are already close to theoretical predictions. This indicates the excellent discovery prospect within the next decade in upcoming detectors such as the gadolinium-loaded SK and JUNO (see, e.g., Beacom & Vagins, 2004; Yüksel et al., 2006; Horiuchi et al., 2009; An et al., 2016; Priya & Lunardini, 2017; Møller et al., 2018).

To exploit the full potential of future observations, comprehensive theoretical models will be needed for comparison. First predictions of the DSNB date back to the 1980s and 1990s (e.g., Bisnovatyi-Kogan & Seidov, 1982; Krauss et al., 1984; Hartmann & Woosley, 1997) and have been refined ever since. Its link to the cosmic history of star formation has been studied in detail (e.g., Ando, 2004; Strigari et al., 2005; Hopkins & Beacom, 2006; Mathews et al., 2014); and also the dependence on the SN source spectra, which will be in the focus of this thesis, has been subject of intense research. For instance, Lunardini (2007) took an analytical approach based on the work by Keil et al. (2003), while Yüksel & Beacom (2007) employed constraints from the measured neutrinos from SN 1987A for their DSNB predictions. The impact of the SN shock revival time has been investigated (Nakazato, 2013; Nakazato et al., 2015), as well as the effect of neutrino flavor conversions (Ando & Sato, 2003; Chakraborty et al., 2011; Lunardini & Tamborra, 2012).

Particularly the contribution from BH-forming, failed explosions to the DSNB has caught much attention in recent years. It might significantly enhance the high-energy tail of the flux spectrum, which is most relevant for the detection (e.g., Lunardini, 2009). Several studies varied

the (still unknown) fraction of failed SNe (Lunardini, 2009; Lien et al., 2010; Keehn & Lunardini, 2012; Priya & Lunardini, 2017; Horiuchi et al., 2018; Møller et al., 2018); in this regard, Nakazato et al. (2015) and Yüksel & Kistler (2015) further considered the cosmic evolution of stellar metallicities; and also the dependence on the high-density equation of state (EoS), which is closely related to the mass limit up to which a NS can be stabilized against its own gravity, has been explored tentatively (Lunardini, 2009; Keehn & Lunardini, 2012; Mathews et al., 2014; Nakazato et al., 2015; Hidaka et al., 2016; Horiuchi et al., 2018).

Detailed neutrino signals from successful and failed SNe are the premise for reliable DSNB predictions. While most previous works employed rather approximate neutrino source spectra, numerical modeling of stellar core collapse has reached a high level of sophistication nowadays. An increasing number of three-dimensional (3D) simulations with detailed microphysics has become available (e.g., Takiwaki et al., 2014; Tamborra et al., 2014; Melson et al., 2015; Lentz et al., 2015; Müller et al., 2017; Ott et al., 2018). Nonetheless, high computational costs are still causing limitations. Up to now, only a few selected progenitors have been considered in 3D SN models, none of them evolved longer than some hundred milliseconds.

At the same time, it was shown that the outcome of a core-collapse event (successful explosion or BH formation) as well as the neutrino emission strongly depend on the progenitor structure, with large variations between different stars (O’Connor & Ott, 2011; Ugliano et al., 2012; Horiuchi et al., 2014; Nakamura et al., 2015; Pejcha & Thompson, 2015; Ertl et al., 2016; Müller et al., 2016; Sukhbold et al., 2016; Ebinger et al., 2018). This has been neglected (or oversimplified) in most previous DSNB studies, which typically employed only a few exemplary models. Particularly the signals from BH-forming, failed SNe are strongly dependent on the progenitor-specific mass-accretion rate (Fischer et al., 2009; O’Connor & Ott, 2011). Comprehensive sets of neutrino signals over the entire range of pre-SN stars are therefore required to adequately account for the diversity of stellar core collapse. In light of this, Horiuchi et al. (2018) employed a set of 101 axisymmetric (2D) SN simulations and seven models of BH formation from spherically symmetric (1D) simulations, however with the need to extrapolate the neutrino signals at times later than  $\sim 1$  s. Due to the limited number of their failed explosions, they (linearly) fitted the spectral parameters of the time-integrated neutrino emission (total energetics, mean energy, and shape parameter) of their few BH simulations as a function of the “progenitor compactness” (O’Connor & Ott, 2011) to account for a larger scope of failed SNe.

In the work at hand, we take a different angle of approach. Referring to the studies by Ugliano et al. (2012), Ertl et al. (2016), and Sukhbold et al. (2016), we use spherically symmetric simulations over a wide range of pre-SN stars exploded by means of a “calibrated central neutrino engine”. In this way, our analysis of the DSNB is based on detailed information on the “landscape” of successful and failed explosions with individual neutrino signals for every progenitor, including cases of long-lasting mass accretion with relatively late BH formation. Using our large sets of (approximately calculated) long-time neutrino signals, which we cross-check by comparing them to the outcome of more sophisticated simulations (see appendix), we aim at providing refined predictions of the DSNB. In a systematic parameter study, we further investigate the impact of three critical source properties on the DSNB flux spectrum: (1) The fractions of successful and failed SNe are varied through different calibrations of the neutrino engine used for the explosion modeling of our large progenitor set. (2) Following the continued mass accretion of failed explosions, we consider different values for the critical mass at which the neutrino signals stop due to BH formation. (3) Based on the study by Keil et al. (2003), we consider different spectral shapes of the neutrino emission.

In our DSNB study, we also include the contribution from electron-capture SNe (ECSNe) of degenerate oxygen-neon-magnesium (ONeMg) cores (Miyaji et al., 1980; Nomoto, 1984, 1987), for which we employ the neutrino signals from Hüdepohl et al. (2010). Moreover, we explore other possible channels for the formation of low-mass NSs, such as accretion-induced collapse (AIC; Bailyn & Grindlay, 1990; Nomoto & Kondo, 1991; Ivanova & Taam, 2004; Hurley et al., 2010; Jones et al., 2016; Wu & Wang, 2018; Ruiter et al., 2018) and merger-induced collapse (MIC; Saio & Nomoto, 1985; Ivanova et al., 2008; Schwab et al., 2016; Ruiter et al., 2018; Kashyap et al., 2018) of white dwarfs (WDs), or ultra-stripped SNe from close binaries (Nomoto et al., 1994; Dewi et al., 2002; Tauris et al., 2013, 2015; Suwa et al., 2015; Müller et al., 2018). Using simplified assumptions, we estimate the flux from such a combined “low-mass component” and comment on its relevance.

## Organization of the Thesis

The thesis is structured as follows. In Chapter 2, we describe the setup of our simulations and discuss the overall properties of the neutrino signals used in our study. Chapter 3 is dedicated to our approach of formulating the DSNB. In Chapter 4, we present the results of our detailed parameter study: We investigate the sensitivity of the DSNB flux spectrum to the fraction of failed explosions, the BH mass threshold, and the spectral shape of the neutrino emission. We further explore an additional contribution from low-mass NS-forming events (such as AIC, MIC, and ultra-stripped SNe) and compare our most extreme models to the Super-Kamiokande flux limits. Our fiducial predictions are discussed in Chapter 5, where we also comment on the impact of neutrino flavor conversions and remaining uncertainties. We summarize our findings and conclude in Chapter 6. Supplementary material can be found in the appendix.

The text of this thesis overlaps in large part with the manuscript for a paper in preparation with Thomas Ertl and Hans-Thomas Janka as coauthors.



# Chapter 2.

## Simulation Setup and Neutrino Signals

In spherical symmetry, self-consistent SN explosions have only been achieved for a few low-mass stars (Kitaura et al., 2006; Janka et al., 2008, 2012; Fischer et al., 2010; Melson et al., 2015; Radice et al., 2017). To still explore the outcome of stellar core collapse in 1D over a wide range of progenitor masses, we adopt the approach of Ertl et al. (2016), where a “calibrated neutrino engine” is placed into the center of all pre-SN models. By this means, we obtain reliable neutrino signals for a large set of individual stars, in good agreement with more sophisticated simulations and including cases of long-term accretion with late BH formation, as we will elaborate in this chapter. For more details on our computational setup, the reader is also referred to Ugliano et al. (2012) and Sukhbold et al. (2016).

### 2.1. Pre-Supernova Models

In this work, we use a combined set of 200 solar-metallicity progenitor models from Woosley & Heger (2007, 2015, “WH07” and “WH15”) and Sukhbold & Woosley (2014, “SW14”), which was already applied in Sukhbold et al. (2016) and can be downloaded from the core-collapse-SN archive of the Garching group<sup>1</sup>. All models are non-rotating single stars, evolved with the KEPLER code (Weaver et al., 1978) up to the onset of iron-core collapse. The resulting grid of progenitors, unevenly distributed over the zero-age main sequence (ZAMS) masses 9 – 120  $M_{\odot}$ , spans the commonly assumed range of “conventional” iron-core collapse SNe (or BH-forming, failed SNe, respectively).

Below that, in the narrow band between 8.7  $M_{\odot}$  and 9  $M_{\odot}$ , we additionally consider ECSNe of degenerate ONeMg cores as another channel for NS formation (Miyaji et al., 1980; Nomoto, 1984, 1987); yet it should be stressed that the exact mass range of ECSNe is unresolved according to current knowledge (see, e.g., Poelarends et al., 2008; Jones et al., 2013; Doherty et al., 2015; Jones et al., 2016). We employ a simulation by H udepohl et al. (2010, “model Sf”) for such core-collapse events. The upper-mass end of the ZAMS mass grid is similarly uncertain and strongly depends on the physics of mass loss. However, as will be detailed in Section 3.2, high-mass contributions are suppressed by the steeply declining initial mass function (IMF) and therefore of subordinate importance for the DSNB.

### 2.2. Supernova Simulations

Our simulations are performed with the PROMETHEUS-HOTB code (Janka & Mueller, 1996; Kifonidis et al., 2003; Scheck et al., 2006; Ertl et al., 2016). The innermost 1.1  $M_{\odot}$  of the nascent proto-NS (PNS) are excised and replaced by a contracting inner-grid boundary and an analytic

---

<sup>1</sup><http://doi.org/10.17617/1.b>

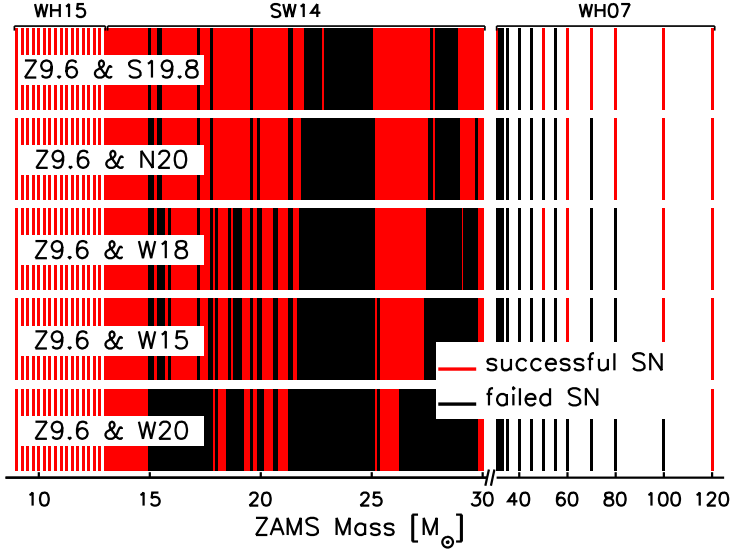


**Figure 2.1.:** “Landscapes of explodability” for our five different calibration models (S19.8, N20, W18, W15, and W20) applied as central engines to the pre-SN stars above  $12 M_{\odot}$ . The low-mass anchor (Z9.6) is the same for all five cases (see main text for details). The ranges of our three progenitor-model sets (WH15, SW14, and WH07) are indicated in the top of the figure. Successful SN explosions are marked in red, while black bars indicate the formation of a BH in a failed SN. From top to bottom, the IMF-weighted fraction of successful explosions decreases from 81.9 % (Z9.6 & S19.8) to 57.6 % (Z9.6 & W20); see Table 2.1. ECSNe are not shown in the plot. (Figure courtesy of Thomas Ertl)

one-zone core-cooling model with tuneable parameters (for the details, see Ugliano et al., 2012). This “central neutrino engine” is calibrated to yield explosions in agreement with the well studied cases of SN 1987A and the Crab SN (SN 1054). More specifically, for pre-SN stars with ZAMS masses above  $12 M_{\odot}$ , which Sukhbold et al. (2016) termed “87A-like”, we apply a PNS core model adjusted such that a given progenitor in the range  $15 - 20 M_{\odot}$ , namely S19.8, N20, W18, W15, or W20 (as described in Sukhbold et al., 2016), reproduces the observed explosion energy ( $\sim 1.5 \times 10^{51}$  erg; Arnett et al., 1989; Utrobin et al., 2015),  $^{56}\text{Ni}$  yield ( $\sim 0.07 M_{\odot}$ ; Bouchet et al., 1991; Suntzeff et al., 1992) and basic neutrino-emission features (Hirata et al., 1987; Bionta et al., 1987) of SN 1987A. The low-mass end ( $9 - 12 M_{\odot}$ ) is connected to the 87A-like cases by an interpolation of the core parameters. As a second anchor point, we use the progenitor Z9.6 by A. Heger (2012, private communication), which explodes with low energy ( $\sim 10^{50}$  erg; Janka et al., 2012; Melson et al., 2015) and a small  $^{56}\text{Ni}$  yield ( $\sim 0.0025 M_{\odot}$ ; Wanajo et al., 2018) in self-consistent simulations, in good agreement with the observational constraints for the Crab SN (Smith, 2013; Tominaga et al., 2013; Yang & Chevalier, 2015). For more details on our calibration procedure, the reader is referred to Sukhbold et al. (2016).

Depending on the calibration model, we obtain more or less successful explosions over the range of considered pre-SN stars, as can be seen in Figure 2.1. While the calibrations S19.8 and N20 lead to the most successful SNe (red), W20 yields a rather weak engine, resulting in a large fraction of BH-forming collapses (black). W18 and W15 reside between these two extremes, as can also be seen in Table 2.1, which shows the IMF-weighted fractions of successful and failed explosions for the different calibration models. The outcome of the low-mass range ( $9 - 12 M_{\odot}$ ) is the same in all five cases, since our interpolation towards Z9.6 is independent of the high-

**Table 2.1.:** Fractions of successful and failed SN explosions resulting from our five sets of calibration models, weighted according to the IMF of Equation (3.5).

Calibration models	successful SNe	failed SNe
Z9.6 & S19.8	81.9 %	18.1 %
Z9.6 & N20	76.9 %	23.1 %
Z9.6 & W18	72.7 %	27.3 %
Z9.6 & W15	70.4 %	29.6 %
Z9.6 & W20	57.6 %	42.4 %

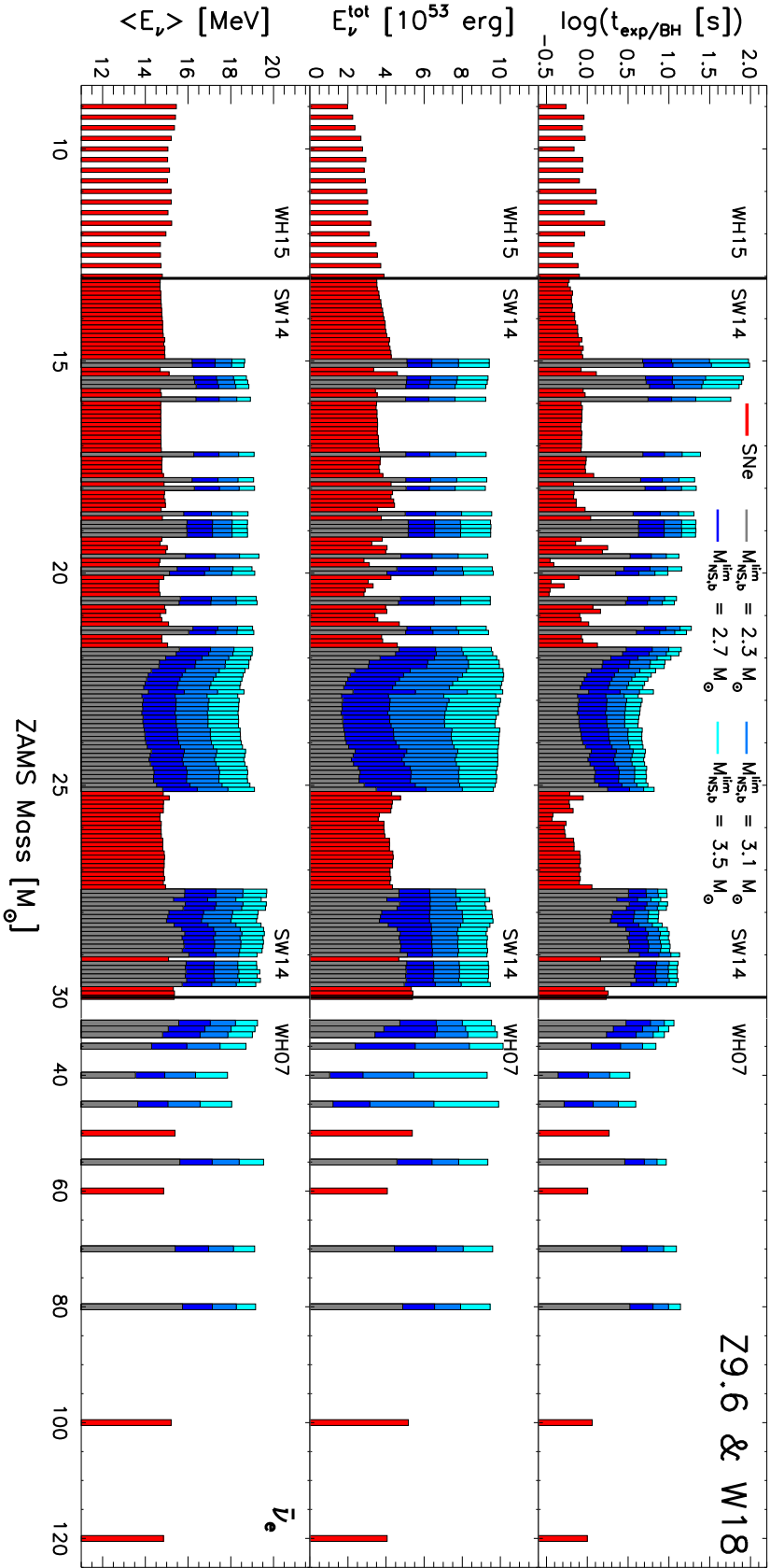
mass calibration. The non-monotonic pattern of successful SNe and BH-forming collapses in Figure 2.1 was described by previous works (Ugliano et al., 2012; Pejcha & Thompson, 2015; Ertl et al., 2016; Müller et al., 2016; Sukhbold et al., 2016; Ebinger et al., 2018). It grounds on the progenitor structure, which is strongly varying with ZAMS mass (O’Connor & Ott, 2011; Horiuchi et al., 2014; Nakamura et al., 2015).

Compared to the simulations of Ertl et al. (2016) and Sukhbold et al. (2016), the neutrino transport outside of the PNS core, which is treated by a gray approximation (Scheck et al., 2006; Arcones et al., 2007), was slightly improved such that we are able to follow cases of long-lasting mass accretion until late collapse to a BH. For numerical reasons, the neutrino-nucleon scattering rate (Equation (D.68) of Scheck et al., 2006) is now split into two separate source terms, one for absorption ( $\propto \langle \epsilon_\nu^4 \rangle$ , with  $\epsilon_\nu$  denoting the neutrino energy) and one for emission ( $\propto T \langle \epsilon_\nu^3 \rangle$ ), to avoid a conversion of sign for large temperatures  $T$ . Furthermore, we implemented an adaptive grid to better resolve the steep density gradients at the PNS surface. Our new code was applied without recalibrating the core models, which led to slightly increased explosion energies (and decreased neutrino luminosities). Accordingly, a few individual progenitors which failed to explode with the old code (cf. Sukhbold et al., 2016, Figure 13) yield successful SNe with our new treatment. In the work at hand, we moreover neglect the late-time fallback of matter pushing a NS beyond the BH limit after a successful explosion was initiated, as such cases turned out to be rare for solar metallicities (Ertl et al., 2016; Sukhbold et al., 2016) and additionally reside in the IMF-suppressed high-mass regime. We thus use the terms “BH formation” and “failed SN” equivalently throughout this work.

## 2.3. Neutrino Signals

For every single progenitor, we obtain time-dependent neutrino luminosities,  $L_{\nu_i}(t)$ , and mean energies,  $\langle E_{\nu_i}(t) \rangle$ , of each neutrino species  $\nu_i = \nu_e, \bar{\nu}_e, \nu_x$ , where  $\nu_x$  denotes a representative heavy-lepton neutrino ( $\nu_\mu, \bar{\nu}_\mu, \nu_\tau, \bar{\nu}_\tau$ ). **Successful SNe** are simulated up to a post-bounce time  $t = 15$  s, when the neutrino luminosities from PNS cooling have already declined to an insignificant level.

In case of **failed explosions**, however, the continued infall of the surrounding mass shells is adding energy to the PNS, leading to an ongoing accretion component of the neutrino luminosities. The signals of such cases are truncated only when the PNS is pushed beyond the (still unknown) limit of BH formation, for which we consider four different values of baryonic mass,  $M_{\text{NS,b}}^{\text{lim}}$  (2.3, 2.7, 3.1, and 3.5  $M_\odot$ ), which are motivated as follows:



Assuming a NS radius of  $(11 \pm 1)$  km<sup>2</sup> and utilizing Equation (36) of Lattimer & Prakash (2001), which we also apply and describe in more detail in Appendix C (see Equation (C.1)), a baryonic NS mass of  $2.3 M_{\odot}$  converts to a gravitating mass of  $1.95^{+0.02}_{-0.03} M_{\odot}$ . This is roughly compatible with the largest currently measured pulsar masses of  $\sim 2 M_{\odot}$  (Demorest et al., 2010; Antoniadis et al., 2013; Özel & Freire, 2016), setting a lower limit for the maximum NS mass. From the first gravitational wave observation of a binary NS merger (GW170817; Abbott et al., 2017a) and its electromagnetic counterparts (Abbott et al., 2017b), Margalit & Metzger (2017) were able to place a tentative upper bound on the maximum gravitational NS mass of  $2.17 M_{\odot}$  (at 90% confidence level). This mass limit is in line with other recent publications (e.g., Shibata et al., 2017; Alsing et al., 2018; Rezzolla et al., 2018; Ruiz et al., 2018). Consistently, we take the baryonic mass  $2.7 M_{\odot}$  (corresponding to  $2.23^{+0.03}_{-0.04} M_{\odot}$  gravitational mass, which is close to this bound) as our reference BH threshold. Nonetheless, Margalit & Metzger (2017) point out several uncertainties related to their analysis. For instance, they neglect the effects of thermal pressure support on the stability of the compact merger remnant, which may change their conclusions. Thermal effects might also be important for the stability of hot PNSs on their way towards BH formation in case of a failed SN, possibly increasing the limiting mass compared to the value for cold NSs (Keil & Janka, 1995; O’Connor & Ott, 2011; Steiner et al., 2013)<sup>3</sup>. For these reasons, we additionally explore two more extreme values,  $3.1 M_{\odot}$  ( $2.50^{+0.04}_{-0.05} M_{\odot}$ ) and  $3.5 M_{\odot}$  ( $2.75^{+0.05}_{-0.05} M_{\odot}$ ) baryonic (gravitating) mass, respectively. Eventually, further pulsar timing measurements (cf. Demorest et al., 2010; Antoniadis et al., 2013; Özel & Freire, 2016) as well as an increased number of observed binary NS mergers should be able to shed more light on the the maximum mass of NSs.

In a few cases, we need to extrapolate our neutrino signals either because the simulations were not carried out to sufficiently late times or due to numerical artifacts, albeit only after  $\sim 10$  s (see Figure A.1). The details are discussed in Appendix A. Furthermore, we should point out that the accretion luminosities of heavy-lepton neutrinos are underestimated compared to  $\nu_e$  and  $\bar{\nu}_e$  in our simulations. This is due to our approximate treatment of the microphysics (nucleon-nucleon bremsstrahlung is not included) as well as due to the relatively modest contraction of the inner-grid boundary and thus underestimated temperatures in the accretion layer. To cure this deficiency, we perform a rescaling of the flavor fractions, as detailed in Appendix B.

In Figure 2.2, we show the outcome systematics of our simulations over the entire range of iron-core progenitors as a function of ZAMS mass, for the exemplary case of the Z9.6 & W18 calibrations, which will serve as a reference in our later discussion (see Chapter 5). The three pre-SN sets WH15, SW14, and WH07 are separated by black vertical lines. Red bars indicate successful explosions, while the outcomes of failed SNe are marked in gray, dark blue, light blue, or cyan, depending on the different choices of the critical baryonic mass for BH formation. In the upper panel, we plot the explosion time,  $t_{\text{exp}}$ , for successful SNe, defined as the time when the shock passes 500 km (and not to confuse with the termination of our SN-neutrino signals at 15 s, which was noted above). In cases of failed explosions, the time of BH formation,  $t_{\text{BH}}$ , is shown, which coincides with a sudden breakdown of the neutrino signal. Depending on the

<sup>2</sup>This range is motivated by recent publications, constraining the NS radius from observations of the binary NS merger event GW170817 (Bauswein et al., 2017; Nicholl et al., 2017; Raithel et al., 2018), as well as by the studies of Özel et al. (2016), Özel & Freire (2016), and Lattimer & Prakash (2016). For NSs at the upper mass end, we consider radii  $10 \text{ km} \leq R_{\text{NS}} \leq 12 \text{ km}$ , while we assume  $R_{\text{NS}} \geq 11 \text{ km}$  in Appendix C for “average-mass” NSs, as suggested by Bauswein et al. (2017).

<sup>3</sup>In fact, it is not clear which of the two competing effects of thermal energy dominates: destabilization due to additional mass-energy or support by thermal pressure.

mass cutoff and the progenitor-dependent mass-accretion rate<sup>4</sup>, these times range from below 1 s up to 100 s in the most extreme cases (note the logarithmic scale). This illustrates the need for a large set of long-time simulations to properly sample the neutrino contribution from the failed channel.

The middle panel of Figure 2.2 shows the total radiated neutrino energies,  $E_{\nu}^{\text{tot}}$ , computed as the time-integrals of the summed-up neutrino luminosities of all species,  $L_{\text{tot}}(t) = L_{\nu_e}(t) + L_{\bar{\nu}_e}(t) + 4L_{\nu_x}(t)$ , from core bounce until termination of the signals. Due to the afore-mentioned numerical improvements in the neutrino transport, these energies are slightly decreased compared to Ertl et al. (2016) and Sukhbold et al. (2016). In Appendix C, we cross-check the values of  $E_{\nu}^{\text{tot}}$  by comparing them to the available budget of gravitational binding energy released during the assembly of the PNS, which we estimate by means of an analytic, radius-dependent description by Lattimer & Prakash (2001). We find good overall agreement, yet we might overestimate the neutrino emission by up to about 10 – 20 % in our simulations, depending on the NS radius. In Chapter 5, we will discuss this and other uncertainties related to our DSNB predictions in more detail. In our work, we neglect neutrino contributions from fallback of matter (after the successful launch of an explosion), since the amount of fallback was shown to be small (typically far below  $10^{-2} M_{\odot}$ ) for most progenitors (Ertl et al., 2016; Sukhbold et al., 2016). At the same time, cases of substantial late-time fallback (possibly turning NSs to BHs) are rare, as noted above.

The mean energies of the time-integrated signals are displayed in the bottom panel of Figure 2.2 for electron antineutrinos, which are most relevant for our study. Values around 15 MeV are the rather uniform outcome of successful SNe, in agreement with other publications (e.g., Mirizzi et al., 2016; Horiuchi et al., 2018). The mean energies from failed explosions, on the other hand, vary considerably among the progenitors and depend strongly on the cutoff mass. Along the way to BH formation, the temperatures within the PNS’s accretion mantle rise gradually, yielding increasingly harder neutrino spectra (see, e.g., Hüdepohl, 2014; Mirizzi et al., 2016).

The neutrino signal of the ECSN by Hüdepohl et al. (2010, “model Sf”) lasts for 8.9 s and yields a total radiated neutrino energy of  $1.63 \times 10^{53}$  erg, with a time-integrated  $\bar{\nu}_e$  mean energy of 11.6 MeV. This is not shown in Figure 2.2, yet we use it for our DSNB analysis, which we describe in the subsequent chapter.

---

<sup>4</sup>Using general-relativistic simulations in spherical symmetry O’Connor & Ott (2011) found a functional dependence of the time to BH formation on the progenitor structure, to first order compliant with a simple power-law scaling:  $t_{\text{BH}} \propto (\xi_{2.5})^{-3/2}$ , where  $\xi_{2.5}$  denotes their compactness parameter at bounce for an enclosed mass of  $2.5 M_{\odot}$ , as defined by their Equation (10). Less compact progenitors of failed SNe, e.g., in the ZAMS mass range around  $15 M_{\odot}$  (see Figure 4 of Ertl et al., 2016), with lower densities in the mass shells surrounding the PNS, need longer accretion times until BH formation, in contrast to the fast-accreting high-compactness progenitors at around  $23 - 24 M_{\odot}$  and  $40 M_{\odot}$ .

## Chapter 3.

### Formulation of the DSNB

The differential number flux,  $d\Phi/dE$ , of DSNB neutrinos and antineutrinos, isotropically impinging on Earth with energy  $E$ , is computed as the line-of-sight integral of the IMF-weighted neutrino spectrum of past core-collapse events ( $dN_{\text{CC}}/dE'$ ; see Sections 3.1 and 3.2) multiplied by the comoving core-collapse rate density ( $R_{\text{CC}}(z)$ ; see Section 3.3) over the cosmic history (e.g., Beacom, 2010):

$$\frac{d\Phi}{dE} = c \int \frac{dN_{\text{CC}}}{dE'} \frac{dE'}{dE} R_{\text{CC}}(z) \left| \frac{dt_c}{dz} \right| dz, \quad (3.1)$$

where  $c$  is the speed of light<sup>5</sup>,  $E' = (1+z)E$  denotes the energy at the time of emission from the corresponding sources at redshift  $z$ , and the term  $|dt_c/dz|$  accounts for the assumed cosmological model, which relates  $z$  to the cosmic time  $t_c$  (see 3.4). In Section 3.5, we consider an additional contribution to the DSNB from low-mass NS-formation events due to an extended ZAMS mass range of ECSNe, as well as due to the possibility of accretion- and merger-induced collapse of WDs and ultra-stripped SNe from close binaries.

#### 3.1. Time-Integrated Neutrino Spectra

For every progenitor, we compute the differential neutrino number spectrum  $d\mathcal{N}/dE$  (in units of  $\text{MeV}^{-1}\text{s}^{-1}$ ) as a function of time  $t$  after core-bounce from the time-dependent luminosity,  $L = L_{\nu_i}(t)$ , and mean energy,  $\langle E \rangle = \langle E_{\nu_i}(t) \rangle$ , of each neutrino species ( $\nu_i = \nu_e, \bar{\nu}_e, \nu_x$ ):

$$\frac{d\mathcal{N}}{dE} = \frac{L}{\langle E \rangle} \frac{f_\alpha(E)}{\int_0^\infty dE f_\alpha(E)}, \quad (3.2)$$

where we assume a spectral shape  $f_\alpha(E)$  according to Keil et al. (2003),

$$f_\alpha(E) = \left( \frac{E}{\langle E \rangle} \right)^\alpha e^{-(\alpha+1)E/\langle E \rangle}. \quad (3.3)$$

In our models, the spectral shape parameter  $\alpha$ <sup>6</sup> is assumed to be constant over time. Although this is a simplification, more sophisticated simulations (e.g., Tamborra et al., 2012; Mirizzi et al., 2016) show that  $\alpha$  does not change dramatically with time, justifying this approximation. Instead, we vary  $\alpha$  as a free parameter over a range of values ( $2 \leq \alpha \leq 4$ ), which we motivate in Appendix D.

<sup>5</sup>Due to their small masses ( $\lesssim 2$  eV; Kraus et al., 2005; Aseev et al., 2011), neutrinos can be approximated to propagate with speed of light.

<sup>6</sup> $\alpha \approx 2.3$  corresponds to a Fermi-Dirac distribution with vanishing degeneracy parameter,  $\alpha > 2.3$  to a pinched, and  $\alpha < 2.3$  to an anti-pinched spectrum;  $\alpha = 2.0$  gives the Maxwell-Boltzmann distribution.

For each progenitor and neutrino species, we then perform a time-integration over the period of emission:

$$\frac{dN}{dE} = \frac{\tilde{\xi}}{\xi} \int dt \frac{d\mathcal{N}}{dE}. \quad (3.4)$$

Because realistic luminosities of the heavy-flavor neutrinos  $\nu_x$  are not available in our sets of simulations due to the approximate micro-physics and the relatively moderate core contraction mentioned in Chapter 2, we rescale each time-integrated spectrum with a factor  $\tilde{\xi}/\xi$  (see Appendix B for the details). By this means, the total radiated neutrino energy  $E_\nu^{\text{tot}}$  is maintained (cf. Appendix C), but redistributed among the species  $\nu_i$  with respective fraction  $\tilde{\xi} = \tilde{\xi}_{\nu_i}$  according to the reference models listed in Table B.1. Correspondingly, the relative fractions before readjustment are denoted as  $\xi = \xi_{\nu_i}$ . In Appendix D, we compare the shapes of our time-integrated spectra with the outcome of more sophisticated simulations by a few exemplary cases to examine the viability of our simplified approach. We find good agreement with these simulations for values of the instantaneous shape parameter  $\alpha$  between 2 and 4.

As mentioned in Chapter 2, our DSNB flux calculations also include the neutrino signal of the  $8.8 M_\odot$ -ECSN simulated by Hüdepohl et al. (2010). The corresponding time-integrated spectra are computed according to Equations (3.2) - (3.4), but with time-dependent shape parameters  $\alpha = \alpha(t)$  as given by the simulation. We use the neutrino data of “model Sf”, which incorporates the full set of neutrino interactions listed in Appendix A of Buras et al. (2006), including nucleon-nucleon bremsstrahlung, making rescaling of the spectra redundant, i.e.,  $\tilde{\xi}/\xi = 1$  for all flavors.

### 3.2. IMF-Weighted Average

The relative abundance of the various pre-SN stars depends on their birth masses. For our DSNB flux predictions, the time-integrated neutrino spectra  $dN/dE$  per core-collapse therefore need to be weighted by an IMF. As in Horiuchi et al. (2011) and Mathews et al. (2014), we apply the modified Salpeter-A IMF of Baldry & Glazebrook (2003),

$$\phi(M) = M^{-\zeta}, \quad (3.5)$$

with  $\zeta = 2.35$  for birth masses  $M \geq 0.5 M_\odot$  and  $\zeta = 1.5$  for  $0.1 M_\odot \leq M < 0.5 M_\odot$ . In our study, we consider masses up to  $125 M_\odot$ , consistent with our choice of the integration normalization in Section 3.3; however, due to the steep decline of Equation (3.5), the high-mass end is suppressed and thus of minor relevance for the DSNB (cf. Hopkins & Beacom, 2006, Section 3).

The IMF-weighted neutrino spectrum  $dN_{\text{CC}}/dE$  of all core-collapse events can then be written as

$$\frac{dN_{\text{CC}}}{dE} = \sum_i \frac{\int_{\Delta M_i} dM \phi(M)}{\int_{8.7 M_\odot}^{125 M_\odot} dM \phi(M)} \frac{dN_i}{dE}, \quad (3.6)$$

where  $\Delta M_i$  denotes the symmetric mass interval around the ZAMS mass  $M_i$  corresponding to the time-integrated spectrum  $dN_i/dE$  of the respective SN, failed-SN, or ECSN simulation<sup>7</sup>. Equation (3.6) is applied separately to all different neutrino species. As in Section 3.1, the

<sup>7</sup>We apply  $\Delta M_i = [(M_{i-1} + M_i)/2, (M_i + M_{i+1})/2]$  for ZAMS masses  $M_i$  with  $9.0 M_\odot < M_i < 120 M_\odot$ ,  $\Delta M_i = [9.0 M_\odot, 9.125 M_\odot]$  for the low-mass end ( $M_i = 9.0 M_\odot$ ) and  $\Delta M_i = [110 M_\odot, 125 M_\odot]$  for the high-mass end ( $M_i = 120 M_\odot$ ) of our iron-core SN/failed-SN grid; whereas for the  $8.8 M_\odot$ -ECSN, we use  $\Delta M_i = [8.7 M_\odot, 9.0 M_\odot]$  as our fiducial range (see Section 2.1).

indices  $\nu_e$ ,  $\bar{\nu}_e$ , and  $\nu_x$  are omitted for the sake of clearness. In the following, we primarily focus on  $\bar{\nu}_e$ , since the prospects for a first detection of the DSNB in upcoming detectors are the best for this species (see, e.g., Beacom & Vagins, 2004; Yüksel et al., 2006; Horiuchi et al., 2009; An et al., 2016). In Section 5.2, we will comment on the heavy-lepton component in view of neutrino flavor oscillations.

### 3.3. Cosmic Core-Collapse Rate

Nuclear burning proceeds fast in massive stars. As a consequence, the progenitors of core-collapse SNe (and failed SNe) have relatively “short” ( $< 10^8$  years) lives compared to cosmological time scales (cf. Kennicutt, 1998). Therefore, the assumption is well justified that the cosmic core-collapse rate density  $R_{CC}(z)$  as a function of redshift equals the birth rate density of stars in the appropriate ZAMS mass range ( $8.7 M_\odot \leq M \leq 125 M_\odot$ ), i.e.,

$$R_{CC}(z) = \psi_*(z) \frac{\int_{8.7 M_\odot}^{125 M_\odot} dM \phi(M)}{\int_{0.1 M_\odot}^{125 M_\odot} dM M \phi(M)} \simeq \frac{\psi_*(z)}{100 M_\odot}. \quad (3.7)$$

Here,  $\psi_*(z)$  denotes the cosmic star formation history (SFH) in units of  $M_\odot \text{Mpc}^{-3} \text{yr}^{-1}$ , which can be deduced from observations (e.g., Hopkins & Beacom, 2006; Reddy et al., 2008; Rujopakarn et al., 2010) and thus is independent of cosmological assumptions. In our study, we adopt the parametrized description by Yüksel et al. (2008),

$$\psi_*(z) = \dot{\rho}_0 \left[ (1+z)^{\alpha\eta} + \left( \frac{1+z}{B} \right)^{\beta\eta} + \left( \frac{1+z}{C} \right)^{\gamma\eta} \right]^{\frac{1}{\eta}}, \quad (3.8)$$

with the best-fit parameters and integration normalization ( $0.1 M_\odot \leq M \leq 125 M_\odot$ ) by Mathews et al. (2014), see Table 1 therein. Even though the uncertainty of the cosmic core-collapse rate is known to be large (its impact on the DSNB flux is discussed in, e.g., Lien et al. 2010), the focus of our work lies on variations of the neutrino source properties. In order to still allow for a range of possible normalizations of  $R_{CC}(z)$ , we additionally employ the  $\pm 1\sigma$  upper and lower limits to the SFH by Mathews et al. (2014), such that we obtain  $R_{CC}(0) = 1.04_{-0.35}^{+0.96} \times 10^{-4} \text{Mpc}^{-3} \text{yr}^{-1}$  for the local universe. The cosmic metallicity evolution and its impact on the DSNB will be briefly discussed in Section 5.3.

For our DSNB calculations, we consider contributions up to a maximum redshift  $z_{\text{max}} = 5$ . However, as it was pointed out in numerous previous works (Ando, 2004; Keehn & Lunardini, 2012; Mathews et al., 2014; Nakazato et al., 2015; Lunardini, 2016), only sources at low redshifts ( $z \lesssim 1 - 2$ ) noticeably add to the high-energy part of the DSNB, which is most relevant for the detection. Neutrinos from higher  $z$  are almost entirely shifted to energies below 10 MeV, where background sources dominate the flux (see, e.g., Lunardini, 2016).

### 3.4. Cosmological Model

Throughout, we assume a standard  $\Lambda$ CDM cosmology with today’s fractions  $\Omega_m = 0.3$  and  $\Omega_\Lambda = 0.7$  of the cosmic energy density in matter and dark energy, respectively, and the Hubble constant  $H_0 = 70 \text{ km s}^{-1} \text{Mpc}^{-1}$ . According to the Friedmann equation, the expansion history

of the Universe is then given by  $dz/dt_c = -H_0(1+z)\sqrt{\Omega_m(1+z)^3 + \Omega_\Lambda}$ . Using this together with Equation (3.1), we can write the DSNB flux spectrum (in units of  $\text{MeV}^{-1}\text{cm}^{-2}\text{s}^{-1}$ ) as

$$\frac{d\Phi}{dE} = \frac{c}{H_0} \int_0^{z_{\max}} \frac{dN_{\text{CC}}}{dE'} \frac{R_{\text{CC}}(z) dz}{\sqrt{\Omega_m(1+z)^3 + \Omega_\Lambda}}. \quad (3.9)$$

We do not vary our cosmological assumptions within this work, like in most publications on the topic. For a recent study on the impact of different cosmological models on the DSNB, the reader is referred to Barranco et al. (2018).

### 3.5. Low-Mass NS-Formation Events

As mentioned above, the low-mass range of core-collapse SN progenitors is rather uncertain. It is widely believed that in degenerate ONeMg cores electron-capture reactions on  $^{20}\text{Ne}$  and  $^{24}\text{Mg}$  can dominate over oxygen deflagration, initiating the collapse to a NS rather than thermonuclear runaway (Miyaji et al., 1980; Nomoto, 1984, 1987). Nevertheless, the exact conditions for such an ECSN to occur in Nature are discussed controversially (see, e.g., Jones et al., 2016). Moreover, it needs to be stressed that we only consider single stars in our study, while observations suggest that most massive stars are in binary systems (see, e.g., Mason et al., 2009; Sana et al., 2012). According to Podsiadlowski et al. (2004), binary interaction might lower the minimum initial mass of a star to form a NS at the end of its life to values as low as  $6 - 8 M_\odot$ , inducing large uncertainties on the DSNB contribution from ECSNe.

In our study, we additionally consider three other formation channels of low-mass NSs, possibly adding to the diffuse neutrino background: electron-capture initiated collapse may also occur when an ONeMg WD is pushed beyond the Chandrasekhar mass limit due to Roche-lobe overflow from a companion. Such a NS-forming event is referred to as AIC (see, e.g., Bailyn & Grindlay, 1990; Nomoto & Kondo, 1991; Ivanova & Taam, 2004; Hurley et al., 2010; Jones et al., 2016; Wu & Wang, 2018; Ruiter et al., 2018). Similarly, Saio & Nomoto (1985) suggested the MIC of two WDs as another possible scenario to form a single NS (also see Ivanova et al., 2008; Schwab et al., 2016; Ruiter et al., 2018). Lastly, close-binary interaction might in some cases lead to the stripping of a stars hydrogen and (most of its) helium envelope onto a companion NS, leaving behind a bare carbon-oxygen star (Nomoto et al., 1994; Dewi et al., 2002), undergoing subsequent iron-core collapse. The explosion of such ultra-stripped SNe (Tauris et al., 2013, 2015; Suwa et al., 2015; Müller et al., 2018) is discussed as the most likely evolutionary pathway leading to the formation of double NS systems (Tauris et al., 2017).

Since not much is known about the rates and detailed source properties of the above-mentioned scenarios, we approach an additional low-mass (LM) contribution to the DSNB by means of simplifying assumptions: We apply a generic neutrino spectrum ( $dN_{\text{LM}}/dE'$ ) adopted from the ECSN by Hüdepohl et al. (2010, “model Sf”) and assume a constant comoving rate density as a function of redshift ( $R_{\text{LM}}(z) = R_{\text{LM}} = \text{const}$ ). In Section 4.3, we vary this unknown rate and investigate the effect of an additional LM component on the DSNB flux spectrum, which can be written in the generalized form

$$\frac{d\Phi}{dE} = \frac{c}{H_0} \int_0^{z_{\max}} dz \frac{R_{\text{CC}}(z) \frac{dN_{\text{CC}}}{dE'} + R_{\text{LM}}(z) \frac{dN_{\text{LM}}}{dE'}}{\sqrt{\Omega_m(1+z)^3 + \Omega_\Lambda}}. \quad (3.10)$$

Having described our computational setup with all its required inputs, we now proceed to the discussion of our results.

# Chapter 4.

## DSNB Parameter Study

In this chapter, we present the results of our detailed DSNB parameter study. First, we give an overview of the single components contributing to the DSNB flux spectrum,  $d\Phi/dE$  (Section 4.1). Using large grids of long-time neutrino signals (cf. Chapter 2), we then probe the sensitivity of the DSNB to three critical source properties (Section 4.2): the fraction of failed explosions (by means of our different calibration models), the threshold mass for BH formation, and the spectral shape of the neutrino emission. Moreover, the possible enhancement of the DSNB by an additional generic “low-mass” component is explored (Section 4.3). In Section 4.4, we compare our most extreme cases with the flux limits placed by the SK experiment.

### 4.1. DSNB Components

In Figure 4.1, we first illustrate how the various sources add to the total DSNB flux spectrum of electron antineutrinos, using our fiducial model (Z9.6 & W18;  $M_{\text{NS,b}}^{\text{lim}} = 2.7 M_{\odot}$ ; best-fit  $\alpha$ ), which we will discuss in more detail in Chapter 5. The left panel shows the individual flux arising from ECSNe, “conventional” iron-core SNe, and BH-forming, failed SNe, respectively (light to dark solid lines). Integrated over all energies, ECSNe contribute only 2.3% ( $0.8 \text{ cm}^{-2}\text{s}^{-1}$ ) to the total flux ( $33.7 \text{ cm}^{-2}\text{s}^{-1}$ ), which is marked by a black dashed line. This value is much lower than the  $\sim 10\%$  suggested by Mathews et al. (2014) as they assumed a considerably wider ZAMS mass range,  $(8 - 10) M_{\odot}$ , compared to  $(8.7 - 9) M_{\odot}$  applied in our work. Above 15 MeV, the component of ECSNe makes up even less than 1% due to its rapidly declining spectrum (cf. low mean energy of 11.6 MeV, as mentioned in Chapter 2). However, since the exact mass window of ECSNe is still unresolved (see, e.g., Poelarends et al., 2008; Jones et al., 2013; Doherty et al., 2015; Jones et al., 2016) and other sources such as ultra-stripped SNe, AIC, and MIC events might contribute to the flux, we consider an increased “low-mass” component in Section 4.3.

“Conventional” iron-core SNe and failed SNe exhibit comparable total fluxes ( $18.6 \text{ cm}^{-2}\text{s}^{-1}$  and  $14.3 \text{ cm}^{-2}\text{s}^{-1}$ , in case of our reference model as shown in Figure 4.1) yet with distinctly different spectral shapes. Below  $\sim 15$  MeV, the contribution from successful explosions prevails, while failed explosions dominate the flux at high energies due to their generally harder spectra (see bottom panel of Figure 2.2). This was pointed out by preceding works (e.g., Lunardini, 2009; Keehn & Lunardini, 2012; Nakazato, 2013; Priya & Lunardini, 2017) and can also be seen in Table 4.1, where we state the flux contributions from the various sources for different ranges of neutrino energies. Between 20 MeV and 30 MeV, failed SNe make up 57% of the total flux (at still higher energies, even 66%). Naturally, these numbers (here, shown for our reference model set) depend strongly on the fraction of failed explosions and their neutrino emission (see Section 4.2). Compared to previous studies, we obtain a generally increased DSNB flux, favorable to its imminent detection. We will comment on this issue more thoroughly below.

**Table 4.1.:** Integrated DSNB flux of electron antineutrinos within the energy ranges (0 – 10) MeV, (10 – 20) MeV, (20 – 30) MeV, and (30 – 40) MeV, for our reference model (Z9.6 & W18;  $M_{\text{NS},b}^{\text{lim}} = 2.7 M_{\odot}$ ; best-fit  $\alpha$ ; see Chapter 5) as shown in Figure 4.1. The relative contributions from the various source types as well as from different redshift intervals are listed.

	(0 – 10) MeV	(10 – 20) MeV	(20 – 30) MeV	(30 – 40) MeV	entire energy range
total DSNB flux ( $\bar{\nu}_e$ )	26.50 /cm <sup>2</sup> /s	6.40 /cm <sup>2</sup> /s	0.70 /cm <sup>2</sup> /s	0.09 /cm <sup>2</sup> /s	33.68 /cm <sup>2</sup> /s
ECSNe	2.6 %	1.1 %	0.5 %	0.2 %	2.3 %
iron-core SNe	56.5 %	51.1 %	42.4 %	33.5 %	55.1 %
failed SNe	40.9 %	47.7 %	57.1 %	66.3 %	42.6 %
0 ≤ z ≤ 1	27.9 %	68.0 %	90.8 %	97.4 %	37.0 %
1 ≤ z ≤ 2	40.5 %	28.9 %	8.9 %	2.4 %	37.6 %
2 ≤ z ≤ 3	19.0 %	2.8 %	0.2 %	< 0.1 %	15.5 %
3 ≤ z ≤ 4	9.9 %	0.3 %	< 0.1 %	< 0.1 %	7.9 %
4 ≤ z ≤ 5	2.8 %	< 0.1 %	< 0.1 %	< 0.1 %	2.2 %

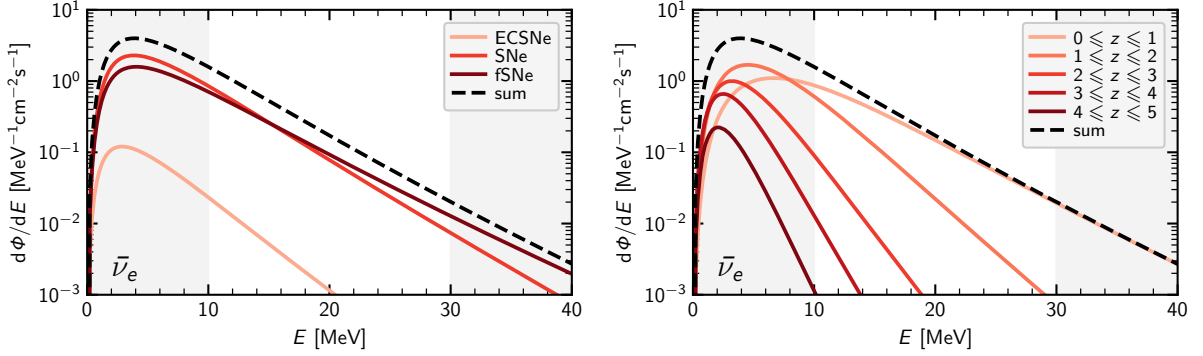


**Figure 4.1.:** Components of the differential DSNB flux,  $d\Phi/dE$ , of electron antineutrinos arriving on Earth with energy  $E$  for the case of our reference model (Z9.6 & W18;  $M_{\text{NS,b}}^{\text{lim}} = 2.7 M_{\odot}$ ; best-fit  $\alpha$ ; see Chapter 5) with  $R_{\text{LM}} = 0$ . In the left panel, solid lines mark the contributions from ECSNe (light), successful iron-core SNe (medium), and failed SNe (dark) to the total DSNB flux (dashed line). The right panel shows the flux originating from different redshift intervals (light to dark, for low to high redshifts, respectively). To guide the eye, the approximate detection window of (10 – 30) MeV is indicated by shaded vertical bands.

In the right panel of Figure 4.1, we compare the DSNB contributions from different redshift intervals (light to dark, for low to high redshifts, respectively). At high energies ( $\gtrsim 20$  MeV), the flux is mainly originating from sources below  $z \sim 1$ , as it was illustrated in several previous works (Ando, 2004; Keehn & Lunardini, 2012; Mathews et al., 2014; Nakazato et al., 2015; Lunardini, 2016). Only at lower energies, the contribution from large redshifts gets increasingly important (see Table 4.1). In both panels of Figure 4.1, shaded bands further indicate the approximate energy window of  $\sim (10 - 30)$  MeV which is most relevant for the DSNB detection in upcoming neutrino observatories. Beyond that, background sources (such as reactor and atmospheric neutrinos) dominate the flux and make any DSNB measurement unfeasible (see, e.g., review by Lunardini, 2016).

As our overall findings apply similarly for all neutrino species, we limit our discussion to electron antineutrinos for now. In Chapter 5, we will comment on the heavy-flavor component (see Table 5.1) in the context of oscillation effects.

## 4.2. DSNB Parameter Dependence

Next, we study how our calibration procedure (as described in Section 2.2), the critical threshold mass for BH formation,  $M_{\text{NS,b}}^{\text{lim}}$ , and the shape parameter  $\alpha$  of the time-dependent neutrino emission impact the DSNB flux spectrum.

In the upper left panel of Figure 4.2, we show  $d\Phi/dE$  for the various choices of models applied to calibrate the central neutrino engine of our simulations. Sets with a higher percentage of failed explosions (see Figure 2.1 and Table 2.1) yield an enhanced DSNB flux, especially in the high-energy regime. This overall picture is in line with the studies by Lunardini (2009), Lien et al. (2010) and Keehn & Lunardini (2012), who varied the fraction of BH-forming collapses while applying generic neutrino spectra and thus neglecting progenitor dependences. More recently, Priya & Lunardini (2017) and Møller et al. (2018) examined the fraction of failed SNe by assuming different ZAMS mass distributions, while Horiuchi et al. (2018), for the first

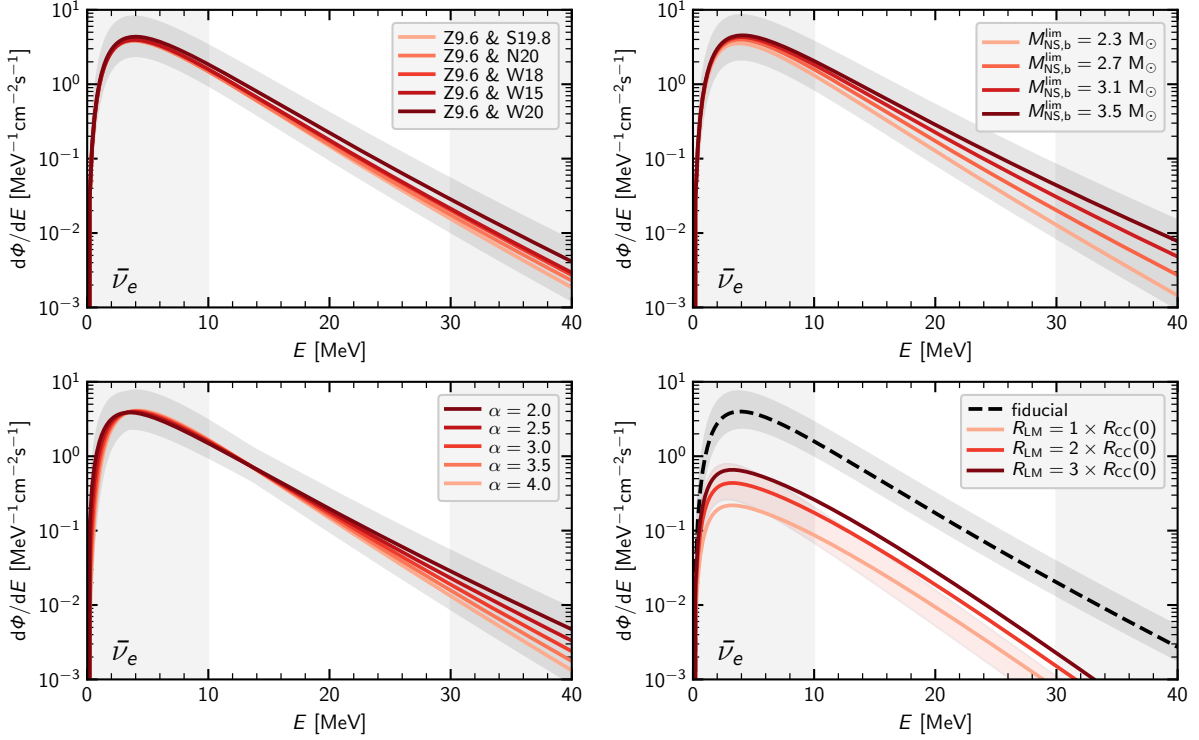


**Figure 4.2.:** Parameter dependence of the DSNB flux spectrum,  $d\Phi/dE$ , for the case of electron antineutrinos. Our calibration models (upper left panel), the BH mass threshold (upper right panel), and the instantaneous shape parameter of the time-dependent neutrino emission (lower left panel) are varied, while keeping all other parameters at their reference values (Z9.6 & W18;  $M_{\text{NS,b}}^{\text{lim}} = 2.7 M_{\odot}$ ; best-fit  $\alpha$ ; see Chapter 5). In the lower right panel, the additional contribution from low-mass (LM) NS-forming events is shown for different constant rate densities  $R_{\text{LM}}$ . For comparison, the pale red band marks the LM flux for an evolving rate instead (see main text for details). Our fiducial model with  $R_{\text{LM}} = 0$  is plotted as dashed line. In each panel, a gray shaded band indicates the uncertainty arising from the cosmic core-collapse rate (corresponding to the  $\pm 1\sigma$  upper and lower limits to the SFH by Mathews et al., 2014). As in Figure 4.1, vertical bands frame the approximate detection window.

time, employed a larger sample of simulations including seven BH cases, thus taking account of progenitor-dependent variations in the neutrino emission from failed explosions (by linearly fitting the total energetics, mean energy, and shape parameter of their time-integrated neutrino spectra as a function of the compactness parameter by O’Connor & Ott 2011; see footnote 4). They explored fractions of BH formation between 0 % and 45 % by taking different values of a threshold compactness above which they assumed their progenitors to form BHs.

Using our large sets of long-time simulations without predefined outcome (also resulting in the BH formation of less compact progenitors with low mass-accretion rates), we can confirm the common result of the previous studies: the larger the fraction of failed explosions, the stronger the enhancement of the DSNB at high energies. To better quantify this behavior, we follow Lunardini (2007) and fit the high-energy tail (20 MeV – 30 MeV) of our DSNB flux spectra with

an exponential function:

$$\frac{d\Phi}{dE} \simeq \phi_0 e^{-E/E_0}. \quad (4.1)$$

Our calibration set Z9.6 & S19.8 with the lowest fraction of failed explosions (18.1%) features the steepest decline (i.e.  $E_0 = 4.4\text{MeV}$ ), while Z9.6 & W20 with 42.4% BH formation yields a flatter spectrum with  $E_0 = 4.8\text{MeV}$ <sup>8</sup>. The “normalization”  $\phi_0$ , on the other hand, is barely affected by our choice of the calibration models. It is instead dominated by the uncertainty arising from the cosmic core-collapse rate, which vertically shifts the entire flux spectrum without changing the slope by more than  $\sim 1\%$ . The gray shaded bands in Figure 4.2 indicate this severe normalization uncertainty (the  $+1\sigma$  upper limit to the SFH of Mathews et al. (2014) is taken for our highest-flux, the  $-1\sigma$  lower limit for our lowest-flux model). The circumstance that the failed-SN fraction is likely to exhibit a dependence on metallicity (and thus redshift) was pointed out by Nakazato et al. (2015) and Yüksel & Kistler (2015). We will come back to this aspect in Chapter 5.

The impact of the high-density EoS on the DSNB has been discussed in the literature to some extent (Lunardini, 2009; Keehn & Lunardini, 2012; Nakazato et al., 2015; Hidaka et al., 2016). Commonly, the spectra from exemplary BH simulations with two different EoS were compared: the stiff Shen EoS (Shen et al., 1998, with incompressibility  $K = 281\text{MeV}$ ) and a softer EoS by Lattimer & Swesty (1991, “LS180” or “LS220”, with  $K = 180\text{MeV}$  or  $K = 220\text{MeV}$ ). Generally, a stiff EoS supports the transiently existing PNS of a failed SN against gravity up to a higher limiting mass than does a soft EoS. The final collapse to a BH therefore sets in after a longer period of mass-accretion and neutrino emission with the consequence of an enhanced DSNB flux and generally higher spectral temperatures.

Having a large compilation of long-time simulations at hand, we take a different (more rigorous) approach in our work: As described in Chapter 2, we directly vary the maximum baryonic PNS mass,  $M_{\text{NS,b}}^{\text{lim}}$ , without assuming a certain EoS. Our neutrino signals from failed explosions are then truncated at this critical threshold for BH formation. In the upper right panel of Figure 4.2, we show the DSNB flux spectra for our various choices of  $M_{\text{NS,b}}^{\text{lim}}$ . Raising the threshold from  $2.3 M_{\odot}$  to  $3.5 M_{\odot}$  drastically enhances the flux towards higher energies, thus lifting the slope  $-(E_0/\text{MeV})^{-1}$  (see Equation (4.1)) from  $-4.3^{-1}$  to  $-5.3^{-1}$ . This strong effect gets immediately clear from Figure 2.2: A higher BH threshold leads to enhanced time-integrated neutrino luminosities and generally hotter spectra, in line with the studies by Lunardini (2009), Keehn & Lunardini (2012), Nakazato et al. (2015), and Hidaka et al. (2016).

We should mention that our work does not consider the possibility of a progenitor-dependent threshold mass for BH formation. O’Connor & Ott (2011) pointed out that thermal pressure support may be stronger for stars with high core compactness, lifting the maximum PNS mass to larger values. This might reduce differences in the neutrino emission among single progenitors; the overall outcome of Figure 4.2 should, however, be unaffected in large part. As we cover a fairly generous margin in our work, the physical values of  $M_{\text{NS,b}}^{\text{lim}}$  as realized for individual PNSs should range somewhere between our extremes. Once the uncertainties affecting the DSNB

<sup>8</sup>For our DSNB models, the parameter  $E_0$  does not have an intrinsically physical interpretation. However, Lunardini (2007) showed that  $E_0$  deviates less than  $\sim 30\%$  from  $\langle E \rangle / (\alpha + 1)$ , for the case that a generic spectrum with shape  $f_{\alpha}$  (Equation (3.3)) is assumed before integrating over redshifts.  $E_0$  can thus be used to compare our DSNB spectra with previous works, which often approximated the source spectrum by means of a characteristic neutrino temperature  $T_{\nu}$  (corresponding to  $\langle E \rangle / (\alpha + 1)$  in case of a vanishing degeneracy parameter).

will be reduced and the maximum mass of a cold NS better constrained, the question of a progenitor-dependent BH threshold can be addressed more thoroughly.

In our study, the spectral shape of the time-dependent neutrino emission is assumed to obey Equation (3.3) with a constant shape parameter  $\alpha$  (for more details, see Appendix D). In the lower left panel of Figure 4.2, we show how the DSNB flux spectrum changes for different choices of  $\alpha$ . As for the source spectra themselves, taking a small  $\alpha$  broadens the shape of the DSNB such that its high-energy tail gets lifted relative to the peak (cf. Keil et al., 2003; Lunardini, 2007, 2016). For  $\alpha = 2.0$ , the exponential fit of Equation (4.1) yields  $E_0 = 5.1$  MeV and  $\phi_0 = 10 \text{ MeV}^{-1}\text{cm}^{-2}\text{s}^{-1}$ . Choosing  $\alpha = 4.0$ , on the other hand, results in a more prominent peak at the cost of a suppressed flux at high energies ( $E_0 = 4.1$  MeV;  $\phi_0 = 19 \text{ MeV}^{-1}\text{cm}^{-2}\text{s}^{-1}$ ). Notice the intersections of the individual curves at  $\sim 3$  MeV and  $\sim 13$  MeV. (Accordingly, we construct the shaded band for the uncertainty of  $R_{\text{CC}}$  such that the lowest-flux model is considered in each segment.)

### 4.3. Additional Low-Mass Component

Here, we assess to what extent an additional contribution from low-mass NS-formation events affects the DSNB. In a footnote, Lien et al. (2010) mentioned that, to a minor degree, neutrinos from the AIC of WDs might add to the total flux, while Mathews et al. (2014) considered SNe of type Ib,c from interacting binaries as a possible source of DSNB neutrinos (however, with the same generic spectrum as for “common” type II SNe). We build upon these tentative assumptions and aim to investigate an additional low-mass channel in a more quantitative way, subsuming the possible contributions from ultra-stripped SNe, AIC, and MIC events (see Section 3.5). To this end, we employ a generic neutrino signal adopted from the ECSN by Hüdepohl et al. (2010, “model Sf”), as the astrophysical community is still lacking sophisticated long-time simulations of AIC, MIC, and ultra-stripped SNe. Nonetheless, it can be expected that the low-mass events considered in our work do not differ in their overall emission properties in a dramatic way. Our approach is therefore meant to serve as an order-of-magnitude estimate, while we naturally cannot capture any details of the underlying physics.

Even more uncertain are the cosmic rates of such events, as a large parameter space in the treatment of binary interaction (especially common-envelope physics) makes precise predictions difficult. Using population synthesis methods, Zapartas et al. (2017) found that core-collapses in binary systems are generally delayed compared to single stars. More particularly, Ruiter et al. (2018) showed that AIC and MIC can proceed in various evolutionary pathways, featuring a variety of delay-times (from below  $10^2$  Myr up to over 10 Gyr) between star burst and eventual core-collapse. For simplicity, we thus explore different values of a comoving rate density,  $R_{\text{LM}}(z) = R_{\text{LM}}$ , which does not change with cosmic time. Further, we examine how our results differ in case of an evolving LM rate.

In the lower right panel of Figure 4.2, we separately plot our fiducial DSNB prediction (dashed line; see Figure 4.1 and Chapter 5) and the additional contribution from LM events for three different constant rate densities  $R_{\text{LM}}$  (solid lines), which we take as multiples of the local core-collapse rate,  $R_{\text{CC}}(0) = 1.04 \times 10^{-4} \text{ Mpc}^{-3}\text{yr}^{-1}$ . As  $R_{\text{CC}}(z)$ , however, strongly varies with redshift (it increases by over an order of magnitude from  $z = 0$  to  $z = 1$ ), we also compute the fraction of the comoving rate densities integrated over the cosmic history:

$$\chi = \frac{\int dz R_{\text{LM}}(z) |dt_c/dz|}{\int dz R_{\text{CC}}(z) |dt_c/dz|}. \quad (4.2)$$

**Table 4.2.:** Contributions from low-mass (LM) NS-formation events (AIC, MIC, and ultrastriped SNe) to the integrated DSNB flux of electron antineutrinos for three different values of the constant rate density  $R_{\text{LM}}$ , given as percentages of our fiducial prediction with  $R_{\text{LM}} = 0$  (cf. Table 4.1). In parantheses, the results from an evolving LM rate with the same  $\chi$  (Equation (4.2)) are given (see main text for details).

	(0 – 10) MeV	(10 – 20) MeV	(20 – 30) MeV	(30 – 40) MeV	entire energy range
fiducial DSNB flux ( $\bar{\nu}_e$ ), $R_{\text{LM}} = 0$	26.50 / cm <sup>2</sup> /s	6.40 / cm <sup>2</sup> /s	0.70 / cm <sup>2</sup> /s	0.09 / cm <sup>2</sup> /s	33.68 / cm <sup>2</sup> /s
$R_{\text{LM}} = 1.0 \times R_{\text{CC}}(0)$ , $\chi = 0.11$	5.6 % (6.1 %)	5.6 % (3.9 %)	4.9 % (2.6 %)	3.1 % (1.4 %)	5.6 % (5.6 %)
$R_{\text{LM}} = 2.0 \times R_{\text{CC}}(0)$ , $\chi = 0.23$	11.3 % (12.2 %)	11.2 % (7.8 %)	9.8 % (5.2 %)	6.1 % (2.9 %)	11.2 % (11.2 %)
$R_{\text{LM}} = 3.0 \times R_{\text{CC}}(0)$ , $\chi = 0.34$	16.9 % (18.3 %)	16.8 % (11.7 %)	14.7 % (7.9 %)	9.2 % (4.3 %)	16.8 % (16.8 %)

This acts as a measure for the ratio of LM events relative to “conventional” core-collapses contributing to the DSNB from the time of redshift  $z = 5$  down to the present day. In Table 4.2, we show the flux contributions from LM events relative to our fiducial model with  $R_{\text{LM}} = 0$  for different energy intervals. To see an effect of at least 10% within the detection window, an additional (constant) low-mass rate  $R_{\text{LM}} = 1.8 \times 10^{-4} \text{ Mpc}^{-3} \text{ yr}^{-1}$  is required, which corresponds to  $\chi = 0.20$ . This is well above realistic estimates for both AIC/MIC events (Metzger et al., 2009; Ruiter et al., 2018) and ultra-stripped SNe (Tauris et al., 2013) of maximally few percent. Any LM contribution to the DSNB is therefore likely to be hidden by the uncertainty arising from the cosmic core-collapse rate (gray shaded band in Figure 4.2).

As a sensitivity check, we additionally consider a comoving rate density,  $R_{\text{LM}}(z)$ , which linearly increases by a factor of 4 between  $z = 0$  and  $z = 1$  and stays constant at even larger redshifts, roughly following the observationally inferred rate of type Ia SNe (e.g., Graur et al., 2011). In the lower right panel of Figure 4.2, the LM-flux contribution resulting from such an evolving rate is indicated by the pale red band (with  $0.11 \leq \chi \leq 0.34$ , like for the three constant rates). The spectra are shifted towards lower energies, as expected due to the relatively increased contribution from high-redshift events. This can also be seen in Table 4.2 (values in parentheses). An enhancement of the differential DSNB flux by 10% at any energy above 10 MeV would even require  $\chi = 0.26$  for an evolving LM rate, which is unreasonably high. Within a realistic detection window, ultra-stripped SNe, AIC, and MIC events should therefore have a negligible effect on the DSNB, unless their cosmic rates are unexpectedly high (no matter how they evolve with redshift). Only when major uncertainties will be reduced significantly, there may be a chance to uncover a contribution to the neutrino background from such low-mass NS-forming events.

#### 4.4. Most Extreme Cases and Comparison with the SK-Flux Limits

After investigating the impact of single source properties on the DSNB in Section 4.2, we now reassess the outcome of our study in the light of the most stringent  $\bar{\nu}_e$ -flux limits set by the SK experiment:  $\Phi_{17.3} \equiv \Phi(E > 17.3 \text{ MeV}) \lesssim (2.8 - 3.1) \text{ cm}^{-2} \text{ s}^{-1}$  (Bays et al., 2012).

The various combinations of our considered parameters lead to a wide spread among the DSNB flux spectra, as can be seen in the left panel of Figure 4.3. At high energies, individual models can differ by over an order of magnitude, with our most extreme cases yielding an integrated flux  $\Phi_{17.3}$  which clearly exceeds the SK limit. To guide the eye, we tentatively mark the region of such disfavored models (with  $\Phi_{17.3} \gtrsim 3.1 \text{ cm}^{-2} \text{ s}^{-1}$ ) by a red shaded band, while the domain of fluxes below  $3.1 \text{ cm}^{-2} \text{ s}^{-1}$  is shown in gray, including our fiducial prediction (dashed line; see Chapter 5). We take the specific model “W18-BH2.7- $\alpha$ 2.0” (short for Z9.6 & W18,  $M_{\text{NS,b}}^{\text{lim}} = 2.7 M_{\odot}$ ,  $\alpha = 2.0$ ) with the upper-limit values of the cosmic core-collapse rate  $R_{\text{CC}}$  (see Section 3.3) as a discriminating line; it yields an integrated flux  $\Phi_{17.3} = 3.16 \text{ cm}^{-2} \text{ s}^{-1}$ , just above the SK limit. We should emphasize, however, that this does not pose a tight boundary, since spectra with very different slopes,  $-E_0^{-1}$  (Equation (4.1)), can yield comparable integrated fluxes in the energy range above 17.3 MeV.

In the right panel of Figure 4.3, we therefore plot  $\Phi_{17.3}$  as a function of the fit parameter  $E_0$  for a selection of models reaching close to (or beyond) the SK bound, which is marked by the red shaded region (with its uncertainty indicated by separate lines). This is further intended to facilitate a comparison with other works (see, e.g., Table 1 in Lunardini & Peres, 2008). The tendency of enhanced integrated fluxes  $\Phi_{17.3}$  for larger values of  $E_0$  gets evident, yet with

#### 4.4. Most Extreme Cases and Comparison with the SK-Flux Limits

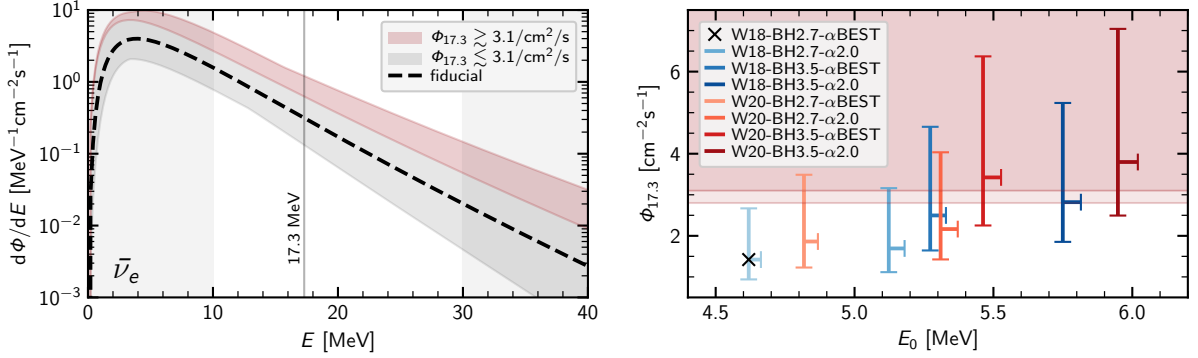


**Figure 4.3.:** Comparison of our most extreme DSNB models with the SK-upper-flux limits:  $\Phi_{17.3} \equiv \Phi(E > 17.3 \text{ MeV}) \lesssim (2.8 - 3.1) \text{ cm}^{-2}\text{s}^{-1}$  (Bays et al., 2012). The shaded bands in the left panel show the spread among the flux spectra,  $d\Phi/dE$ , of electron antineutrinos, resulting from various combinations of the source parameters considered in Section 4.2 (see Figure 4.2). Our fiducial model (W18-BH2.7- $\alpha$ BEST; Chapter 5) is marked by a dashed line. To guide the eye, we separately show the approximate ranges for models which yield an integrated flux  $\Phi_{17.3}$  below  $3.1 \text{ cm}^{-2}\text{s}^{-1}$  (gray) or exceeding it (red); see the main text for details. As in Figures 4.1 and 4.2, vertical bands frame the approximate detection window. In the right panel, the scatter of  $\Phi_{17.3}$  is shown for a selection of models (including our fiducial case; black cross) reaching close to or beyond the SK limits (pale and dark shaded for  $2.8$  and  $3.1 \text{ cm}^{-2}\text{s}^{-1}$ , respectively) as a function of the fit parameter  $E_0$  (Equation (4.1)); both vertical and horizontal error bars indicate the uncertainty arising from the cosmic SFH.

significant scatter. Especially the large uncertainties arising from the cosmic core-collapse rate, as indicated by error bars, smear this trend. Nonetheless, the most extreme combinations of our considered parameters, such as W20-BH3.5, featuring a strong contribution from failed SNe and thus large  $E_0$  (see Section 4.2), are already disfavored, with  $\Phi_{17.3}$  reaching well beyond the SK limit (unless a minimal  $R_{CC}$  is taken). Even a less extreme baryonic threshold mass or calibration model can still lead to an integrated flux in excess of the SK bound: both W20-BH3.1- $\alpha$ 2.0 and W15-BH3.5- $\alpha$ 2.0, neither of which shown in Figure 4.3, still yield  $\Phi_{17.3} = 2.9_{-1.0}^{+2.5} \text{ cm}^{-2}\text{s}^{-1}$ , with a predominant fraction of the  $\bar{\nu}_e$  (79 % and 74 %, respectively) originating from BH-formation events.

Unlike in Malek et al. (2003), the limits given by Bays et al. (2012) are model-dependent. Nevertheless, for an energy threshold close to  $\sim 20 \text{ MeV}$ , the flux limits are rather insensitive to the spectral shape as pointed out by Lunardini & Peres (2008). In any case, our models fall within the range of spectral temperatures ( $3 \text{ MeV} \leq T_\nu \leq 8 \text{ MeV}$ ; see footnote 8) which was considered by Bays et al. (2012). Repeating their analysis with our DSNB spectra should therefore lead to comparable flux limits. For illustration, we simply apply the bound  $(2.8 - 3.1) \text{ cm}^{-2}\text{s}^{-1}$  independently, to all our models, as it is shown in Figure 4.3. Naturally, this cannot replace a sophisticated statistical analysis, which is beyond the scope of this work.

Our fiducial model (W18-BH2.7- $\alpha$ BEST) yields an integrated flux of  $\Phi_{17.3} = 1.4_{-0.5}^{+1.2} \text{ cm}^{-2}\text{s}^{-1}$ , which is just below the SK bound, possibly with even less than a factor of two difference. Intriguingly, Bays et al. (2012) pointed out that there might already be a hint of a signal in the SK-II and SK-III data, making hope that the first detection of the DSNB is just coming within reach (cf. Beacom & Vagins, 2004; Yüksel et al., 2006; Horiuchi et al., 2009; Keehn & Lunardini,

#### *Chapter 4. DSNB Parameter Study*

2012; An et al., 2016; Priya & Lunardini, 2017). In the subsequent chapter, we will describe our best predictions in more detail and also comment on remaining uncertainties. After a discussion of neutrino flavor conversions (Section 5.2) we will get back to the comparison of our models with the SK bound.

# Chapter 5.

## Fiducial DSNB Predictions and Remaining Uncertainties

In this Chapter, we comment on the parameter choices for our fiducial DSNB model and investigate the impact of neutrino flavor conversions. Moreover, we discuss the remaining uncertainties of our predictions and compare our results with other recent DSNB studies.

### 5.1. Fiducial Parameter Choices

In Section 2.2, we described the calibration procedure for the central neutrino engine of our simulations. As our reference case we take the intermediate Z9.6 & W18 calibration, like in Ertl et al. (2016) and Sukhbold et al. (2016). The resulting nucleosynthesis yields show a fairly reasonable agreement with the solar element abundances (when type Ia SNe are included); and the NS mass distribution roughly fits observational data (Özel & Freire, 2016), as does the distribution of BH masses (Wiktorowicz et al., 2014) if one assumes that only the star’s helium core collapses while its hydrogen envelope gets unbound (cf. Nadezhin, 1980; Lovegrove & Woosley, 2013; Kochanek, 2014; Adams et al., 2017). For more details, the reader is referred to Sukhbold et al. (2016). The fraction of failed explosions (27 %; see Table 2.1) is still rather high for Z9.6 & W18, but not unrealistic given the large discrepancy between the observed SN rate and the SFH (Horiuchi et al., 2011). And also the recent discovery of a disappearing star (Kochanek et al., 2008; Adams et al., 2017) supports a non-zero fraction of failed explosions.<sup>9</sup>

For the baryonic PNS threshold mass (above which our neutrino signals are truncated), we take the fiducial value of  $M_{\text{NS,b}}^{\text{lim}} = 2.7M_{\odot}$ , which converts to  $2.23_{-0.04}^{+0.03}M_{\odot}$  gravitating mass (when a NS radius of  $(11 \pm 1)$  km is assumed; see Equation (C.1)). As we mentioned in Section 2.3, this is close to the upper bound placed by Margalit & Metzger (2017) from observations of the GW170817 event and its associated kilonova (Abbott et al., 2017a,b). The limit by Margalit & Metzger (2017) follows from their argumentation that the merger outcome was a relatively short-lived, differentially-rotating hyper-massive NS, disfavoring both the prompt collapse to a BH as well as the formation of a long-lived, supra-massive NS. The value further matches other recent publications (e.g., Shibata et al., 2017; Alsing et al., 2018; Rezzolla et al., 2018; Ruiz et al., 2018).

The spectral shapes of the neutrino emission are explicitly discussed in Appendix D. Our time-integrated spectra match the outcome of more sophisticated simulations best, if we take an instantaneous shape parameter  $\alpha = 3.2$  for our successful SNe with baryonic NS masses of

---

<sup>9</sup>Our most extreme calibration, Z9.6 & W20, which is yielding by far the largest fraction of failed SNe (42 %; see Table 2.1), is disfavored since it would lead to a significant underproduction of s-process elements (Brown & Woosley, 2013; Sukhbold et al., 2016).

$M_{\text{NS,b}} \leq 1.6 M_{\odot}$ , and  $\alpha = 2.7$  for SNe with  $M_{\text{NS,b}} > 1.6 M_{\odot}$  as well as for the failed explosions. This “best-fit” choice for  $\alpha$ , together with our reference calibration Z9.6 & W18,  $M_{\text{NS,b}}^{\text{lim}} = 2.7 M_{\odot}$ , and the best-fit parameters for the cosmic SFH by Mathews et al. (2014), marks our fiducial model, which was already referenced in Chapter 4.

## 5.2. Neutrino Flavor Conversions

So far, we only considered the DSNB flux of electron antineutrinos, as their discovery prospects in upcoming detectors are the best (see, e.g., Beacom & Vagins, 2004; Yüksel et al., 2006; Horiuchi et al., 2009; An et al., 2016; Priya & Lunardini, 2017; Møller et al., 2018). However, on their way out of a star, neutrinos (and antineutrinos) undergo collective and matter-induced (MSW) flavor conversions (Wolfenstein, 1978; Mikheyev & Smirnov, 1985; Duan et al., 2010). Hereafter, we discuss how such oscillations can affect our DSNB flux predictions.

Following Chakraborty et al. (2011) and Lunardini & Tamborra (2012), we write the DSNB flux spectrum of electron antineutrinos after including the effect of flavor conversions as

$$\frac{d\Phi_{\bar{\nu}_e}}{dE} = \bar{p} \frac{d\Phi_{\bar{\nu}_e}^0}{dE} + (1 - \bar{p}) \frac{d\Phi_{\nu_x}^0}{dE}, \quad (5.1)$$

where  $d\Phi_{\bar{\nu}_e}^0/dE$  and  $d\Phi_{\nu_x}^0/dE$  are the unoscillated spectra for electron antineutrinos ( $\bar{\nu}_e$ ) and a representative heavy-lepton neutrino ( $\nu_x$ ).  $\bar{p} \simeq 0.7$  ( $\bar{p} \simeq 0$ ) denotes the survival probability for  $\bar{\nu}_e$  in case of normal (NH) or inverted (IH) mass hierarchy, respectively<sup>10</sup>. Recently, Møller et al. (2018) confirmed that this simplified description holds for the set of simulations from the Garching group which they used in their study and which also serve as reference models in our work (see Table B.1 in Appendix B). We already mentioned earlier that our setup does not provide reliable information on the heavy-flavor channel, which is why we rescale the relative energy outcome of the single neutrino species (see Section 3.1). For the same reason, we also adjust the spectral parameters ( $\langle E_{\nu_x} \rangle$  and  $\alpha_{\nu_x}$ ) of the time-integrated  $\nu_x$  emission, guided by the simulations listed in Table B.1, to get a more realistic prediction of  $d\Phi_{\nu_x}^0/dE$  (see Appendix B for the details).

In the left panel of Figure 5.1, we show the unoscillated DSNB spectra,  $d\Phi_{\bar{\nu}_e}^0/dE$  (black dashed line) and  $d\Phi_{\nu_x}^0/dE$  (red solid line), for our fiducial model parameters. According to Equation (5.1), the latter marks the case of IH, where a complete flavor swap ( $\bar{\nu}_e \leftrightarrow \nu_x$ ) takes place. If, instead, the NH is realized in Nature, an outcome between the two plotted extremes can be expected. The uncertainty arising from the cosmic core-collapse rate is indicated by shaded bands. In Table 5.1, we additionally state the integrated flux of  $\nu_x$  for different energy ranges, as it was shown in Table 4.1 for the case of  $\bar{\nu}_e$ . The most prominent difference is a reduced contribution from failed SNe, which gets clear from the small heavy-flavor fractions  $\tilde{\xi}_{\nu_x}$  of the two reference models for BH formation, which we employ for our rescaling (Appendix B). At the

<sup>10</sup>Lunardini & Tamborra (2012) showed that the effects of self-induced (collective) conversions and the MSW resonances can be treated separately, as the latter occurs further out from the central core regions of a SN. The  $\bar{\nu}_e$  survival probability is then given by  $\bar{p} = \cos^2 \theta_{12} \bar{P}_c$  for NH, and  $\bar{p} = \cos^2 \theta_{12} (1 - \bar{P}_c)$  for IH, with  $\bar{P}_c$  denoting the survival probability after collective effects only (for more details, also see Chakraborty et al., 2011). However, Lunardini & Tamborra (2012) noted that self-induced conversions affect the DSNB only at the few-percent level and can therefore be neglected. Also the recently discussed fast conversions (see, e.g., Chakraborty et al., 2016; Tamborra et al., 2017; Izaguirre et al., 2017), which might lead to partial flavor equilibration, should not shift the DSNB beyond the two discussed extremes of purely MSW-enhanced conversions (i.e.,  $\bar{p} \simeq 0$  and  $\bar{p} \simeq 0.7$ ), as pointed out by Møller et al. (2018).

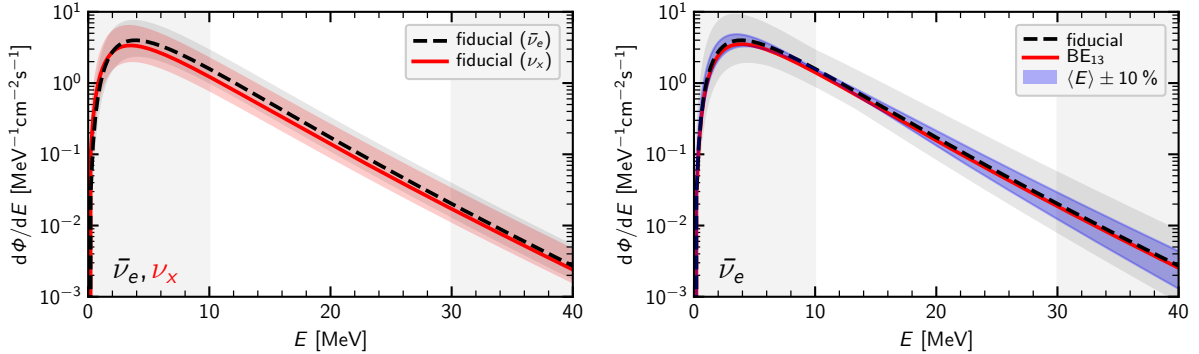


**Figure 5.1.:** Fiducial predictions of the DSNB flux spectrum  $d\Phi/dE$  (model W18-BH2.7- $\alpha$ BEST; cf. Figures 4.1-4.3) and remaining uncertainties. The left panel shows the spectra of both electron antineutrinos ( $\bar{\nu}_e$ ; black dashed line) and a representative heavy-lepton (anti)neutrino ( $\nu_x$ ; red solid line), with the uncertainty arising from the cosmic core-collapse rate,  $R_{CC}$ , indicated by shaded bands. In the right panel, our fiducial model (black dashed line;  $\bar{\nu}_e$ ) is compared to a flux spectrum where the total radiated neutrino energy of each successful SN is adjusted to match the respective gravitational binding energy  $BE_{13}$  (Equation (C.1)) of the left-behind NS, assuming a radius of 13 km (red solid line). The blue shaded band marks the range of spectra for which the time-integrated neutrino mean energies  $\langle E \rangle$  (of both successful and failed SNe) are shifted by  $\pm 10\%$ ; see the main text for details. The additional uncertainty due to  $R_{CC}$  is shown as a gray band.

same time, the contribution from successful explosions (including ECSNe) is largely unchanged, which reflects their approximate flavor equipartition.

Despite the less dominant contribution from failed SNe, the slope  $-(E_0/\text{MeV})^{-1}$  of the exponential tail (see Equation (4.1)) is slightly lifted from  $-4.6^{-1}$  to  $-4.7^{-1}$  in case of a complete flavor swap, because smaller shape parameters  $\alpha$  (see Table B.1;  $\lambda_\alpha < 1$ ) are partly compensating the reduced flux in the high-energy tail. The mean energies of the time-integrated neutrino signals are fairly similar for  $\nu_x$  and  $\bar{\nu}_e$  (see Table B.1;  $\lambda_E \sim 1$ ), as suggested by state-of-the-art simulations (e.g., Marek et al., 2009; Müller & Janka, 2014). On the contrary, several previous DSNB studies employed spectra with  $\langle E_{\nu_x} \rangle \gg \langle E_{\bar{\nu}_e} \rangle$  (particularly for the emission from failed explosions). Hüdepohl (2014) surmised that this difference may be caused by a simplified (iso-energetic) treatment of the neutrino-nucleon opacities used in previous works.

In line with the recent studies by Priya & Lunardini (2017) and Møller et al. (2018), we find that neutrino flavor conversions exert a fairly moderate influence on the DSNB, which is well hidden by other uncertainties. Nonetheless, for our highest-flux models, which are largely dominated by the contribution from BH-forming events, the oscillation effects become more pronounced. For this reason, we reconsider our comparison with the SK-flux limits (see Section 4.4): In case of IH, the integrated flux of our most extreme model set (W20-BH3.5- $\alpha$ 2.0) above 17.3 MeV decreases by 36% from  $\Phi_{17.3} = 3.8_{-1.3}^{+3.2} \text{cm}^{-2}\text{s}^{-1}$  to  $\Phi_{17.3} = 2.4_{-0.8}^{+2.1} \text{cm}^{-2}\text{s}^{-1}$ , below the SK bound (however, note the large uncertainties due to the cosmic core-collapse rate). At the same time, the exponential fit parameter  $E_0$  changes by less than 0.1%. For NH, we obtain  $\Phi_{17.3} = 3.4_{-1.2}^{+2.9} \text{cm}^{-2}\text{s}^{-1}$ , which is still above the SK limits<sup>11</sup>. Apparently, the large degeneracies

<sup>11</sup>In case of our fiducial model, the effects of flavor conversions are less distinct, as described above (see left panel of Figure 5.1 and Table 5.1). The flux  $\Phi_{17.3}$  decreases by only 6% (19%) for NH (IH), still reaching close to the SK bound.

**Table 5.1.:** Integrated DSNB flux of a representative heavy-lepton neutrino ( $\nu_x$ ) within the energy ranges (0 – 10) MeV, (10 – 20) MeV, (20 – 30) MeV, and (30 – 40) MeV, for our reference model (W18-BH2.7- $\alpha$ BEST): cf. Table 4.1, where the  $\bar{\nu}_e$  flux is shown. The relative contributions from the various source types (ECSNe; successful iron-core SNe; failed SNe) are listed.

	(0 – 10) MeV	(10 – 20) MeV	(20 – 30) MeV	(30 – 40) MeV	entire energy range
total DSNB flux ( $\nu_x$ )	22.54 /cm <sup>2</sup> /s	5.00 /cm <sup>2</sup> /s	0.57 /cm <sup>2</sup> /s	0.07 /cm <sup>2</sup> /s	28.18 /cm <sup>2</sup> /s
ECSNe	3.0 %	1.5 %	0.8 %	0.4 %	2.7 %
iron-core SNe	67.9 %	64.8 %	56.8 %	48.0 %	67.1 %
failed SNe	29.1 %	33.8 %	42.4 %	51.6 %	30.3 %

among the parameters entering our flux calculations still render both precise predictions and the exclusion of models difficult (cf. Møller et al., 2018).

### 5.3. Remaining Uncertainties

As pointed out in Appendix C, the total radiated neutrino energies ( $E_\nu^{\text{tot}}$ ) of our successful SNe might, on average, be overestimated by a few percent. In the right panel of Figure 5.1, we therefore compare our fiducial DSNB prediction (black dashed line) with a model where  $E_\nu^{\text{tot}}$  of all exploding progenitors is adjusted to match the gravitational binding energy  $\text{BE}_{13}$  of the corresponding NS remnants (Equation (C.1) with  $R_{\text{NS}} = 13$  km), which reduces the contribution from successful SNe by 24.4 % (red solid line). Since a considerable fraction of the flux is originating from failed explosions, the difference between the two lines is barely visible on the logarithmic scale. For an assumed NS radius of 11 or 12 km, the deviation gets even less.

A stronger effect can be seen if we instead vary the mean energies,  $\langle E \rangle$ , of the time-integrated spectra by  $\pm 10$  % for both successful and failed SNe, as indicated by the blue shaded band. Particularly at high energies, the spectra diverge noticeably. Such a range of uncertainty cannot be ruled out according to present knowledge. In Appendix D, we show that the outcome of our simplified approach is in reasonable overall agreement with more sophisticated simulations; nonetheless, the mean energies of the time-integrated spectra do not fully overlap (see Table D.1). Apart from that, we should emphasize that the neutrino emission characteristics strongly depend on the still unknown high-density EoS (e.g., Marek et al., 2009). Moreover, Bollig et al. (2017) showed that the inclusion of muons, which was so far neglected in numerical simulations, can further raise the neutrino energies.

Despite these inherent uncertainties of the neutrino source spectra, the cosmic core-collapse rate,  $R_{\text{CC}}$ , still constitutes the largest uncertainty affecting the DSNB, especially at lower energies (cf. Horiuchi et al., 2009; Nakazato et al., 2015). Accordingly, the gray shaded band in the right panel of Figure 5.1 indicates the  $\pm 1\sigma$  variation of  $R_{\text{CC}}$  (cf. left panel and Figure 4.2) on top of the uncertainty arising from  $\langle E \rangle$  of the source spectra (blue shaded band). While the approximate redshift dependence of the cosmic SFH (and thus core-collapse rate) is rather well known (e.g., Hopkins & Beacom, 2006; Yüksel et al., 2008), its normalization is still inducing significant uncertainties to the DSNB. Using the parametrization by Yüksel et al. (2008) together with the fit parameters by Mathews et al. (2014), we obtain a local core-collapse rate density  $R_{\text{CC}}(0) = 1.04^{+0.96}_{-0.35} \times 10^{-4} \text{Mpc}^{-3} \text{yr}^{-1}$ , as described in Section 3.3. Upcoming wide-field surveys such as LSST (Tyson, 2002) should be able to pin down the *visible* SN rate (below redshifts  $z \sim 1$ ) to good accuracy, opening the chance for DSNB measurements to probe particularly the contribution from *faint* and *failed* explosions (Lien et al., 2010).

After all, one should keep in mind that we only employ solar-metallicity progenitor models in our simulations. Evidently, this is a simplification, as the distribution of metals in the Universe is spatially non-uniform (see, e.g., the low metallicities in the Magellanic Clouds) and evolves with cosmic time. It can further be expected that the fraction of failed explosions depends on metallicity (e.g., Heger et al., 2003). For these reasons, Nakazato et al. (2015) and Yüksel & Kistler (2015) considered a failed-SN fraction which increases with redshift. On the other hand, Panter et al. (2008) suggested that the average metallicity does not decline dramatically up to  $z \sim 2$ . Assuming solar metallicities therefore should be a sufficiently good approximation, considering that the DSNB flux above a realistic detection threshold is almost entirely arising from sources at moderate redshifts (see Figure 4.1).

At this point we should also remind the reader that a core-collapse SN is an inherently multi-dimensional phenomenon (see, e.g., Müller, 2016). While our simplified 1D approach should be able to capture the overall picture of the progenitor-dependent neutrino emission, an increasing number of fully self-consistent 3D simulations will need to confirm our findings eventually.

## 5.4. Comparison with Previous Works

Lastly, we compare our DSNB flux predictions with the outcome of other recent works. For instance, Priya & Lunardini (2017) found a  $\bar{\nu}_e$  component above 11 MeV in the range  $(1.4 - 3.7) \text{ cm}^{-2}\text{s}^{-1}$ , with their highest-flux model being a factor of  $\sim 3$  below the SK limit by Bays et al. (2012). Our fiducial model in contrast yields  $5.4_{-1.9}^{+4.6} \text{ cm}^{-2}\text{s}^{-1}$  ( $4.6_{-1.6}^{+3.9} \text{ cm}^{-2}\text{s}^{-1}$ ) above 11 MeV in case of normal (inverted) mass hierarchy, reaching very close to the SK bound (see Sections 4.4 and 5.2). Likewise, the recent study by Møller et al. (2018) suggested a clearly less prominent DSNB compared to our work (see their Figures 3 and 10). These differences in the flux can be understood in terms of the diverse neutrino outcome of our simulations, as shown in Figure 2.2. While progenitors at the very low end of the ZAMS mass grid radiate  $E_{\nu}^{\text{tot}} \simeq 2 \times 10^{53} \text{ erg}$ , the emission increases to values of  $(3 - 4) \times 10^{53} \text{ erg}$  for progenitors still well below  $15 M_{\odot}$ . On the other hand, Priya & Lunardini (2017) and Møller et al. (2018) apply the neutrino signals of the low-energetic ( $E_{\nu}^{\text{tot}} \simeq 2 \times 10^{53} \text{ erg}$ ) s11.2c and z9.6co models for the entire (IMF-enhanced) low-mass domain. Moreover, both studies make use of failed-SN models which form BHs relatively fast ( $\lesssim 2 \text{ s}$ ) and therefore radiate less energy ( $\lesssim 3.7 \times 10^{53} \text{ erg}$ ) than most of our failed explosions. Each of these two aspects makes for a reduction of the integral flux by some ten percent compared to our work.

Horiuchi et al. (2018) for the first time employed a larger set of neutrino signals in their DSNB study, including seven models of BH-forming, failed explosions. However, the total neutrino energies  $E_{\nu}^{\text{tot}}$  radiated from their failed SNe lie commonly below  $\sim 3.5 \times 10^{53} \text{ erg}$ , even when linearly extrapolated to the lowest considered threshold compactness  $\xi_{\text{crit}} = 0.1$  (see their Figure 5). By contrast, we find total neutrino energies from failed explosions up to  $5.2 \times 10^{53} \text{ erg}$  for a mass threshold at  $M_{\text{NS,b}}^{\text{lim}} = 2.3 M_{\odot}$  and even up to  $6.7 \times 10^{53} \text{ erg}$  in case of our fiducial value,  $M_{\text{NS,b}}^{\text{lim}} = 2.7 M_{\odot}$  (see Figures 2.2 and C.2), enhancing the integral flux by some ten percent compared to Horiuchi et al. (2018). Accordingly, our study suggests that particularly the inclusion of slowly-accreting progenitors with late BH formation (not considered in previous works) makes for a significant contribution to the DSNB.

# Chapter 6.

## Summary and Conclusions

Using large sets of long-time neutrino signals from spherically symmetric SN simulations over a wide range of progenitors, we presented refined predictions for the DSNB. In a systematic parameter study, we further investigated how its flux spectrum depends on three crucial source properties: the fraction of failed explosions, the threshold mass for BH formation, and the spectral shape of the neutrino emission. Beyond that, we explored a still uncertain component of low-mass NS-forming events such as AIC and MIC of WDs, and ultra-stripped SNe from close binaries.

Different from previous works, our approach includes detailed information on the success or failure of explosions over the entire ZAMS mass range ( $9 - 120 M_{\odot}$ ) of our 200 considered pre-SN models (see Figure 2.1). For every progenitor, we obtained an individual neutrino signal, which lasts for several seconds. This enabled us not only to follow the PNS cooling of successful SNe until late times, but also to track the continued accretion of failed explosions up to an parameterized (because uncertain) mass limit for BH formation. Especially progenitors of failed SNe with relatively low core compactness (which have not been considered in previous studies) may radiate total neutrino energies in clear excess of their exploding counterparts, depending on the assumed BH threshold mass (see Figure 2.2), with noticeable implications for the DSNB.

By means of applying different calibration models to the central neutrino engine of our 1D explosion simulations, we confirmed the basic result of previous works (e.g., Lunardini, 2009): An increased fraction of failed explosions enhances the DSNB towards higher energies, flattening the decline of the nearly exponential tail (see upper left panel of Figure 4.2). Going beyond the studies by Lunardini (2009), Keehn & Lunardini (2012), Nakazato et al. (2015), and Hidaka et al. (2016), all of which considered only exemplary cases of BH formation for different high-density EoSs, we found a strong dependence of the DSNB flux spectrum on the maximum NS mass, with a spread of almost an order of magnitude at high energies (Figure 4.2; upper right panel). The main contribution to this enhanced signal originates from non-exploding progenitors with long accretion times before the PNS collapses to a BH (see Figures 2.2 and C.2).

Moreover, we investigated how the spectral shape of the instantaneous neutrino emission from a core-collapse event (which we assumed to obey the functional form of Keil et al. 2003; see Equation (3.3)) affects the DSNB flux spectrum: As for the source spectra themselves, taking a shape parameter  $\alpha \sim 2$  leads to a broader integral spectrum than larger  $\alpha$ -values, enhancing the high-energy part at the cost of a reduced peak (Figure 4.2; lower left panel). However, all these variations are dominated by the major uncertainty arising from the cosmic core-collapse rate.

In addition to “conventional” iron-core SNe, ECSNe, and BH-forming, failed explosions, we also considered a possible DSNB contribution from ultra-stripped SNe, AIC, and MIC events. Under the simplifying assumptions of a generic source spectrum adopted from an ECSN simulation (Hüdepohl et al., 2010) and a constant (or linearly increasing with redshift) cosmic rate density,

we found that the effect of such an additional “low-mass channel” on the DSNB can be neglected above a realistic detection threshold of  $\sim 10$  MeV, unless the underlying rates are unexpectedly high (see lower right panel of Figure 4.2 and Table 4.2).

Intriguingly, our reference model predicts a DSNB flux which clearly exceeds the outcome of previous works (see Section 5.4), mainly due to the inclusion of failed explosions with late BH formation and, consequently, long-lasting neutrino emission. Our fiducial predictions therefore reach close to the SK-flux limit by Bays et al. (2012). This raises the hope for an imminent DSNB discovery with the aid of upcoming detectors (e.g., Beacom & Vagins, 2004; An et al., 2016). One should, however, bear in mind that large uncertainties (particularly the normalization of the cosmic SFH) still render precise predictions impossible (see the large spread in Figures 4.3 and 5.1). While our description of the DSNB is based on approximate models, it should still be able to capture the overall picture of the diverse neutrino emission from stellar core collapses. We cross-checked our results with an analytic description by Lattimer & Prakash (2001) for the available budget of gravitational binding energy (Appendix C) as well as with more sophisticated simulations of successful and failed SNe (Appendix D). Eventually, a large set of fully self-consistent 3D simulations (including more detailed studies of late BH-formation events) will have to confirm our preliminary findings.

In line with the studies by Priya & Lunardini (2017) and Møller et al. (2018), we found that our fiducial predictions are weakly affected by neutrino flavor conversions: Within the detection window, the flux of electron antineutrinos is reduced by less than  $\sim 7\%$  ( $\sim 23\%$ ) in the case of NH (IH) compared to the case of no oscillations (see Section 5.2). Only for the most extreme models with the highest contribution from failed explosions, the reduction may become as large as  $\sim 36\%$  for the case of a complete flavor swap (IH) because of a lower fraction of energy released in heavy-lepton neutrinos. Note that we employ spectra for the heavy-flavor channel which feature mean energies comparable to electron antineutrinos, whereas several previous DSNB studies assumed  $\langle E_{\nu_x} \rangle \gg \langle E_{\bar{\nu}_e} \rangle$ , which might be a consequence of the non-inclusion of energy-exchanging neutrino-nucleon scattering (see, e.g., Janka, 2017).

Within our study, we scanned large parts of the parameter space governing the DSNB source spectra. Our most extreme models yield a flux right on the edge of (or even beyond) the existing SK bound. Directly constraining individual unknowns from a non-detection is, however, still hampered by large degeneracies. Nevertheless, it can be expected that some of the physical quantities entering the DSNB predictions will be better constrained in the not too distant future: an increasing number of gravitational-wave observations from binary-NS mergers (Abadie et al., 2010) will yield more information on the maximum mass and the radius of NSs, placing tighter constraints on the high-density EoS; long-baseline (oscillation) experiments should be able to determine the neutrino mass hierarchy (e.g., LBNE Collaboration et al., 2013); and upcoming wide-field surveys such as LSST (Tyson, 2002) will measure the rate of *visible* SNe (below  $z \sim 1$ ) to good accuracy.

At the same time future observations of the DSNB will probe the *entire* population of stellar core collapse in its full diversity, particularly including *faint* and *failed* explosions (cf. Lien et al., 2010). This opens the chance to better constrain the cosmic core-collapse rate as well as the the fraction of BH-forming, failed SNe (Møller et al., 2018). Moreover, the DSNB may even carry the imprint of new physics (e.g., Farzan & Palomares-Ruiz, 2014; Jeong et al., 2018). These exciting prospects, for both particle and astrophysics, motivate ongoing efforts to steadily improve the theoretical predictions of the DSNB.

# Appendix A.

## Extrapolation of neutrino signals

In our analysis as described in Chapters 2 and 3, we employ the neutrino signals from successful SNe up to 15 s post bounce, when their luminosities have declined to an insignificant level. The signals from failed explosions are instead required to reach the BH threshold mass,  $M_{\text{NS,b}}^{\text{lim}}$ , which may take tens of seconds in case of low mass-accretion rates and high  $M_{\text{NS,b}}^{\text{lim}}$  (see upper panel of Figure 2.2). Not all of our simulations were carried out long enough because of rising computational costs or due to numerical artifacts emerging at late times (after several seconds). We thus extrapolate these neutrino signals after their termination at post-bounce time  $t_0$ . In the upper panel of Figure A.1,  $t_0$  is plotted against ZAMS mass for our reference calibrations Z9.6 & W18. Typically, our extrapolation starts at around 8 – 10 s, whereas no extrapolation was needed for a few single SNe at the low-mass end and for our fast-accreting failed SNe (cf. top panel of Figure 2.2). Even if the exact values of  $t_0$  are slightly different for our other calibration models, the overall picture remains the same.

The cooling phases of our successful, NS-forming SNe are well described by an exponential decline of the neutrino signal at sufficiently late times after shock revival, when the mass accretion onto the hot PNS has ceased and the diffusion of neutrinos from the core defines the emission (cf. Müller et al., 2016). We thus extrapolate the signals of our successful SNe according to

$$L_{\text{core}}(t) = L_0^{\text{core}} e^{-(t-t_0)/\tau} \quad (\text{A.1})$$

for all neutrino species  $\nu_i$ , with  $L_0^{\text{core}} = L_{\nu_i}(t_0)$ , the corresponding luminosity at time  $t_0$ , and a core-cooling timescale  $\tau = \tau_{\nu_i}$ , which we each obtain from a least-squares fit over the last 2 s. Our values for  $\tau$  typically range between 1 and 4 s, in agreement with the work by Hüdepohl (2014) (also see Müller et al., 2016, Table 1). The lower panel of Figure A.1 shows the relative contribution to the total radiated neutrino energy from our extrapolation. It lies below  $\sim 2\%$  for all SNe (independently of the calibration). The neutrino mean energies,  $\langle E_{\nu_i}(t) \rangle$ , are simply extrapolated by keeping them constant at their final values at  $t_0$  (cf. Horiuchi et al., 2018).

In case of a BH-forming, failed SN on the other hand, the continued infall of matter feeds an ongoing accretion luminosity in addition to the diffusive radiation from the core (Burrows, 1988). Therefore, we describe the total neutrino emission as the sum of a core and an accretion component,  $L_{\text{tot}}(t) = L_{\text{core}}(t) + L_{\text{acc}}(t)$ . For the accretion luminosity, we follow the description by Burrows (1988),

$$L_{\text{acc}}(t) = \eta \frac{GM_{\text{NS,b}}(t)\dot{M}_{\text{NS,b}}(t)}{R_{\text{NS}}(t)}, \quad (\text{A.2})$$

with the gravitational constant  $G$  and an adjustable efficiency parameter  $\eta$  (cf. Fischer et al., 2009; Hüdepohl, 2014; Müller & Janka, 2014). For computational reasons, we take the late-time evolution of the progenitor-dependent (baryonic) PNS mass,  $M_{\text{NS,b}}(t)$ , and accretion rate,  $\dot{M}_{\text{NS,b}}(t)$ , from pure hydrodynamic simulations with switched-off neutrino engine and an open

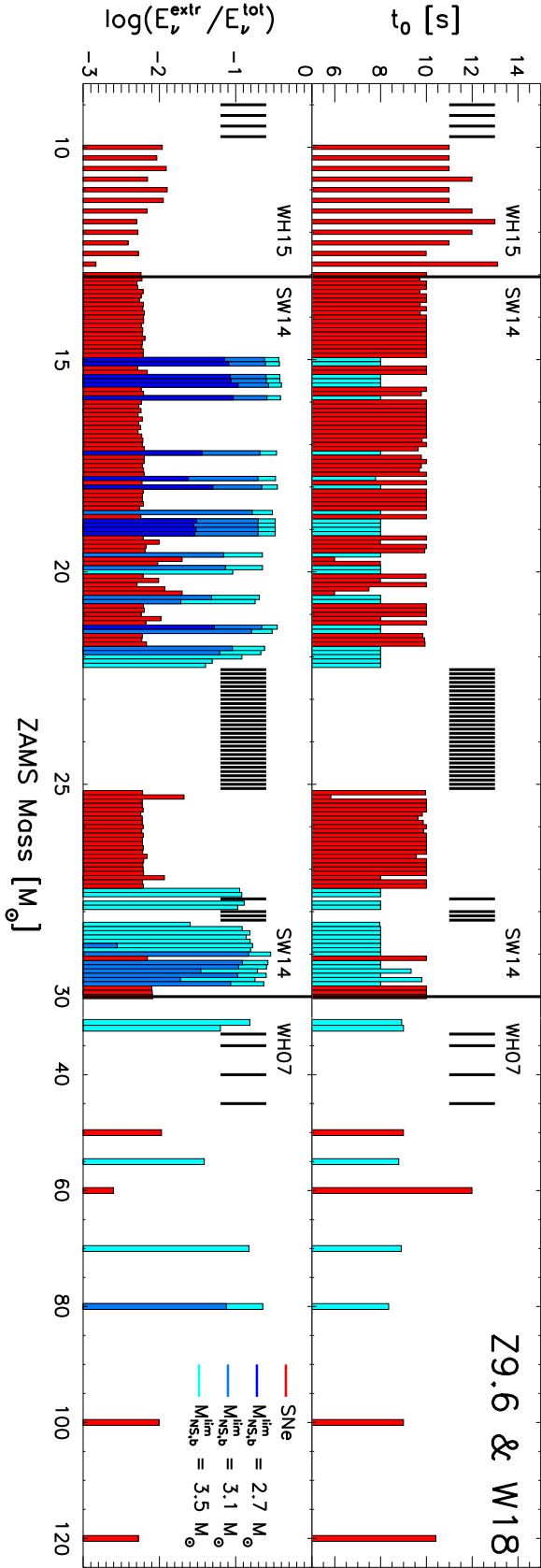


**Figure A.1.:** Systematics of our signal extrapolation over the range of progenitor models from the WH15, SW14, and WH07 sets for the case of the Z9.6 & W18 calibrations (cf. Figure 2.2). In the upper panel, the starting time of our extrapolation,  $t_0$ , is given. The lower panel shows the relative fraction of the total radiated neutrino energy arising from the extrapolation (note the logarithmic scale). Both quantities are plotted versus ZAMS mass. Red bars indicate successful SN explosions, while BH-forming, failed SNe are marked in dark blue, light blue, and cyan corresponding to a BH mass threshold at  $2.7 M_{\odot}$ ,  $3.1 M_{\odot}$ , and  $3.5 M_{\odot}$ , respectively (no extrapolation was needed for the case of  $2.3 M_{\odot}$ ). The time  $t_0$  is independent of the mass cutoff. Cases without extrapolation are indicated by black vertical lines. (Figure courtesy of Thomas Ertl)

inner boundary in the regime of supersonically infalling matter (outside of the shock). As we do not have reliable information on the time-dependent radius,  $R_{\text{NS}}(t)$ , of the contracting PNS, we adopt Equation (9) of Müller et al. (2016),

$$R_{\text{NS}}(t) = \left[ R_1^3 \left( \frac{\dot{M}_{\text{NS,b}}(t)}{M_\odot \text{ s}^{-1}} \right) \left( \frac{M_{\text{NS,b}}(t)}{M_\odot} \right)^{-3} + R_0^3 \right]^{1/3}. \quad (\text{A.3})$$

We find that the late phases of our failed-SN simulations which are carried out beyond 10 s (21 cases in the N20 and 72 in the W20 set, 17 of them beyond 20 s) are reproduced by Equations (A.2) and (A.3) with an accuracy of few percent if we choose the parameters  $R_1 = 40$  km,  $R_0 = 11$  km<sup>12</sup> and an accretion efficiency  $\eta = 0.51$ . Similar values for  $\eta$  were found by Fischer et al. (2009), Hübepohl (2014), and Müller & Janka (2014). We apply this description of the accretion luminosity to all of our extrapolated failed-SN signals, independently of the calibration. For the core luminosity from failed explosions, we employ Equation (A.1) with an initial value  $L_0^{\text{core}} = L_{\text{tot}}(t_0) - L_{\text{acc}}(t_0)$  and a core-cooling timescale  $\tau = \tau_{\nu_x}$  ( $\sim 1$  s) from a least-squares fit of each heavy-flavor signal between 3 s and 6 s after bounce. During this phase,  $L_{\nu_x}$  is dominated by its core component and well described by an exponential decline. We hence take it as a measure also for the core luminosity of electron-type neutrinos, which is not as readily accessible (cf. Hübepohl, 2014; Müller & Janka, 2014). The flavor ratio of the single luminosity components is kept constant at its final value at the end of each simulation ( $L_{\bar{\nu}_e}(t_0) : L_{\nu_e}(t_0) : L_{\nu_x}(t_0)$ )<sup>13</sup>.

As can be seen in the lower panel of Figure A.1, our extrapolation accounts for up to  $\sim 40\%$  of the total radiated neutrino energy for a BH limit at  $3.5 M_\odot$  in the most extreme cases, while no extrapolation was required for a mass cutoff at  $2.3 M_\odot$ . This is true for all our calibration sets. The neutrino mean energies from slowly-accreting failed SNe, which rely on an extrapolation the most, flatten to rather constant values ( $\sim 20$  MeV) in the late phases (after  $\sim 10$  s) of our simulations. We thus extrapolate the mean energies of failed SNe constantly with their final values at  $t_0$ , as done in the case of successful SNe. We tested other extrapolation schemes, but found that the time-integrated spectra are largely insensitive to the late-time description of the mean energies.

<sup>12</sup>The absolute values of  $R_1$  and  $R_0$  can be chosen somewhat arbitrarily since the adjustable parameter  $\eta$  compensates for shifts of  $L_{\text{acc}}$  in Equation (A.2). For consistency, we take  $R_0 = 11$  km (see footnote 2). The resulting best-fit value  $R_1 = 40$  km is relatively small compared to 120 km in Müller et al. (2016), which reflects the moderate core contraction in our simulations.

<sup>13</sup>In one single failed-SN case (s27.4 of the W20 set), the simulation terminates at 4.49 s (the earliest  $t_0$  among all our 948 signals) when the core luminosity still dominates the signal of heavy-lepton neutrinos over its accretion component, while electron-type neutrinos are already defined by  $L_{\text{acc}}$ . Here, we first extrapolate the heavy-flavor component according to Equation (A.1) up to 7 s and apply the sum of an accretion and a core component for all flavors only above this time.



## Appendix B.

### Flavor rescaling

Our approximate treatment of the microphysics and the relatively modest contraction of our inner-grid boundary result in underestimated luminosities of the heavy-flavor neutrinos, as mentioned in Chapters 2 and 3. Consequently, we introduced a rescaling factor  $\tilde{\xi}/\xi$  for the time-integrated neutrino spectra in Equation (3.4), where  $\xi = \xi_{\nu_i}$  and  $\tilde{\xi} = \tilde{\xi}_{\nu_i}$  denote the relative fractions of the total neutrino energy  $E_{\nu}^{\text{tot}}$  radiated in the species  $\nu_i$ , before and after readjustment, respectively. As reference cases, we employ six successful explosion models and two failed SNe, which are simulated with the 1D-version of the PROMETHEUS-VERTEX code (Rampp & Janka, 2002) and are listed in Table B.1: z9.6co and s27.0co, each with the LS220 (Lattimer & Swesty, 1991) and the SFHo EoS (Steiner et al., 2013) employed, which were already discussed in detail in Mirizzi et al. (2016); the unpublished model s20.0 by R. Bollig (2018, private communication; s20-2007 progenitor from Woosley & Heger, 2007) with the SFHo EoS, simulated in the same way as the four models above<sup>14</sup>; and the three models s11.2co, s40.0c, and s40s7b2c by Hüdepohl (2014), each with the LS220 EoS. The neutrino signals of all eight models can be found in the core-collapse-SN archive of the Garching group<sup>15</sup>.

While we confine ourselves to the  $\bar{\nu}_e$  component in large part, we need information on the time-integrated spectra,  $dN_{\nu_x}/dE$ , of heavy-lepton neutrinos for our discussion of flavor oscillations in Section 5.2. Instead of taking the outcome of our simulations, we directly employ the spectral shape by Keil et al. (2003),

$$\frac{dN_{\nu_x}}{dE} = \frac{(\alpha_{\nu_x} + 1)^{(\alpha_{\nu_x} + 1)}}{\Gamma(\alpha_{\nu_x} + 1)} \frac{E_{\nu_x}^{\text{tot}}}{\langle E_{\nu_x} \rangle^2} \left( \frac{E}{\langle E_{\nu_x} \rangle} \right)^{\alpha_{\nu_x}} \exp \left[ -\frac{(\alpha_{\nu_x} + 1)E}{\langle E_{\nu_x} \rangle} \right], \quad (\text{B.1})$$

with the total energy radiated in a single heavy-flavor species,  $E_{\nu_x}^{\text{tot}} = \tilde{\xi}_{\nu_x} E_{\nu}^{\text{tot}}$ , the neutrino mean energy,  $\langle E_{\nu_x} \rangle = \lambda_E \langle E_{\bar{\nu}_e} \rangle$ , and the shape parameter,  $\alpha_{\nu_x} = \lambda_{\alpha} \alpha_{\bar{\nu}_e}$ . Here,  $\langle E_{\bar{\nu}_e} \rangle$  and  $\alpha_{\bar{\nu}_e}$  are computed from the time-integrated spectra of electron antineutrinos as from our simulations (Equations (D.1)-(D.3)). For the conversion factors  $\lambda_E \equiv \langle E_{\nu_x} \rangle / \langle E_{\bar{\nu}_e} \rangle$  and  $\lambda_{\alpha} \equiv \alpha_{\nu_x} / \alpha_{\bar{\nu}_e}$ , we take the values from the VERTEX models in Table B.1.

The neutrino spectra of our successful explosions which are forming NSs with baryonic mass  $M_{\text{NS,b}} \leq 1.6 M_{\odot}$  are rescaled by the average conversion factors of the s11.2co and the two z9.6co models (upper part of Table B.1). For SNe with  $M_{\text{NS,b}} > 1.6 M_{\odot}$ , we apply the average of the s20.0 and s27.0co models (middle part of Table B.1). In case of failed explosions, forming BHs (lower part of Table B.1), we distinguish between fast-accreting ( $t_{\text{BH}} < 2$  s) and slowly-accreting ( $t_{\text{BH}} \geq 2$  s) cases. The spectra of our fast-accreting models (progenitors of high core compactness; see footnote 4) are rescaled according to s40s7b2c, which forms a BH after 0.57 s.

<sup>14</sup>The simulation applies a mixing-length treatment of convection (“c”) and includes the nucleon background potentials in the neutrino-nucleon opacities (“o”). For the details, see Mirizzi et al. (2016).

<sup>15</sup><https://wwwmpa.mpa-garching.mpg.de/ccsnarchive/archive.html> (access provided upon request)

**Table B.1.:** Relative fractions  $\xi_{\bar{\nu}_e}$ ,  $\xi_{\nu_e}$ , and  $\xi_{\nu_x}$  of the total energy  $E_\nu^{\text{tot}}$  radiated in the species  $\bar{\nu}_e$ ,  $\nu_e$ , and  $\nu_x$ , and conversion factors  $\lambda_E \equiv \langle E_{\nu_x} \rangle / \langle E_{\bar{\nu}_e} \rangle$  and  $\lambda_\alpha \equiv \alpha_{\nu_x} / \alpha_{\bar{\nu}_e}$ , resulting from our eight reference models, simulated with the 1D-version of PROMETHEUS-VERTEX. The single entries are grouped according to their compact remnants (see text for the details). Note that  $\xi_{\nu_e} + \xi_{\bar{\nu}_e} + 4\xi_{\nu_x} = 1$ .

Model	$\xi_{\bar{\nu}_e}$	$\xi_{\nu_e}$	$\xi_{\nu_x}$	$\lambda_E$	$\lambda_\alpha$	Compact Remnant	$M_{\text{NS,b}} [M_\odot]$
VERTEX, s11.2co, LS220	0.166	0.194	0.160	0.990	0.808	NS	1.366
VERTEX, z9.6co, LS220	0.155	0.173	0.168	0.992	0.810	NS	1.361
VERTEX, z9.6co, SFHo	0.157	0.176	0.167	0.990	0.790	NS	1.363
average	0.159	0.181	0.165	0.991	0.803	—	—
VERTEX, s20.0, SFHo	0.172	0.176	0.163	0.965	0.813	NS	1.947
VERTEX, s27.0co, LS220	0.172	0.181	0.162	0.957	0.807	NS	1.776
VERTEX, s27.0co, SFHo	0.170	0.179	0.163	0.973	0.810	NS	1.772
average	0.171	0.179	0.163	0.965	0.810	—	—
VERTEX, s40s7b2c, LS220	0.212	0.257	0.133	1.068	0.639	BH (fast; 0.57 s)	(2.320)
VERTEX, s40.0c, LS220	0.231	0.251	0.129	0.940	0.724	BH (slow; 2.11 s)	(2.279)

For our slowly-accreting BH cases with relatively lower core compactness (or higher baryonic mass cutoff), we employ the rescaling factors of model s40.0c with BH formation at  $t_{\text{BH}} = 2.11\text{ s}$ . For completeness, we also give the baryonic PNS masses right before the BH collapse in Table B.1. Note that approximate flavor equipartition ( $\tilde{\xi}_{\bar{\nu}_e} \simeq \tilde{\xi}_{\nu_e} \simeq \tilde{\xi}_{\nu_x}$ ) is realized for successful SNe, while  $\bar{\nu}_e$  and  $\nu_e$  dominate over heavy-lepton neutrinos in case of failed explosions. This is due to the continued infall of matter, which is accompanied by  $e^\pm$  captures on free nucleons in the PNS's accretion mantle (Janka, 2012), giving rise to an enhanced accretion luminosity (see Equation (A.2)) of electron-flavor (anti)neutrinos.



## Appendix C.

### Total energies of radiated neutrinos

In both successful and failed core-collapse SNe, the neutrino emission is fed by the release of gravitational binding energy (BE) from an assembling PNS, which either cools down to a stable NS or further collapses to a BH. To assess the viability of our DSNB flux predictions, we thus compare the total radiated neutrino energy,  $E_\nu^{\text{tot}}$ , of our simulations with an analytic expression for the BE. For this purpose, we adopt Equation (36) of Lattimer & Prakash (2001), which connects the PNS's baryonic mass,  $M_{\text{NS,b}}$ , with its gravitating mass,  $M_{\text{NS,g}}$ , assuming a final (cold) NS radius  $R_{\text{NS}}$ :

$$\frac{\text{BE}/c^2}{M_{\text{NS,g}}} = \frac{0.6\beta}{1 - 0.5\beta} \quad , \quad (\text{C.1})$$

with  $\text{BE}/c^2 \equiv M_{\text{NS,b}} - M_{\text{NS,g}}$  and the dimensionless parameter  $\beta \equiv GM_{\text{NS,g}}/R_{\text{NS}}c^2$ .

In the left panel of Figure C.1,  $E_\nu^{\text{tot}}$  of our successful explosions in the Z9.6 & W18 set is plotted against the baryonic mass of the formed NS (turquoise dots). We compare it with the corresponding gravitational binding energies  $\text{BE}_{11}$  and  $\text{BE}_{12}$  (black and red dashed lines), computed according to Equation (C.1) with an assumed final NS radius of 11 km and 12 km,

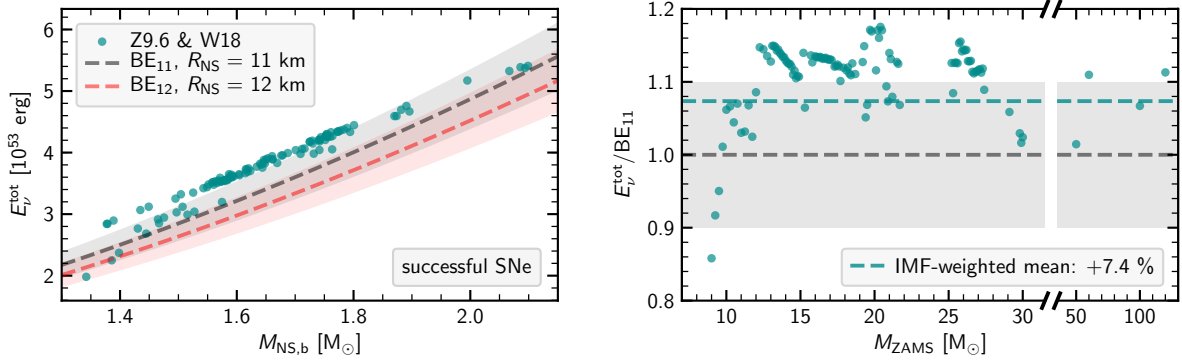


**Figure C.1.:** Comparison of the total neutrino energy,  $E_\nu^{\text{tot}}$ , radiated from the successful explosions of our reference set (Z9.6 & W18) with the gravitational binding energy (BE) of the left-behind NS as per an analytic description by Lattimer & Prakash (2001). In the left panel, the relation of  $E_\nu^{\text{tot}}$  and the baryonic NS mass,  $M_{\text{NS,b}}$ , is shown (turquoise dots). The black (red) dashed line indicates the NS's binding energy as a function of  $M_{\text{NS,b}}$ , computed according to Equation (C.1) with an assumed radius of 11 km (12 km). The shaded bands correspond to deviations of  $\pm 10\%$ . In the right panel, the ratio of the total radiated neutrino energy and BE is plotted versus ZAMS mass for a NS radius of 11 km. The dashed turquoise line additionally indicates the IMF-weighted mean value of  $+7.4\%$  relative to BE. Note the scale break at  $M_{\text{ZAMS}} \sim 30 M_\odot$ .

Appendix C. Total energies of radiated neutrinos

**Table C.1.:** IMF-weighted deviations of  $E_{\nu}^{\text{tot}}$  from the analytic descriptions of the gravitational binding energies  $\text{BE}_{11}$ ,  $\text{BE}_{12}$ , and  $\text{BE}_{13}$  as per Equation (C.1) for our five sets of calibration models, assuming a final NS radius of 11 km, 12 km, and 13 km, respectively.

Calibration models	$R_{\text{NS}} = 11 \text{ km}$	$R_{\text{NS}} = 12 \text{ km}$	$R_{\text{NS}} = 13 \text{ km}$
Z9.6 & S19.8	+12.1 %	+21.0 %	+29.9 %
Z9.6 & N20	+6.4 %	+14.8 %	+23.3 %
Z9.6 & W18	+7.4 %	+15.9 %	+24.4 %
Z9.6 & W15	+5.4 %	+13.7 %	+22.1 %
Z9.6 & W20	+7.4 %	+15.9 %	+24.5 %

respectively (see footnote 2). The shaded bands indicate deviations of  $\pm 10\%$  from this analytic description. In the right panel, we further show the ratio of the total radiated neutrino energy and BE for the case of  $R_{\text{NS}} = 11 \text{ km}$ , plotted against the progenitors’s zero-age main sequence mass  $M_{\text{ZAMS}}$ .

Our simulations feature good overall agreement with Equation (C.1), conformable to the PNS of a successful SN radiating essentially its entire energy budget in the form of neutrinos. Assuming a NS radius of 11 km, 93 % of the successful explosions in our calibration set Z9.6 & W18 deviate less than 15 % from the description by Lattimer & Prakash (2001). While most of our simulations overestimate the total radiated neutrino energy in the order of 10 %, the dominant part of low-mass progenitors exhibits energies close to or even below  $\text{BE}_{11}$ , leading to an IMF-weighted mean deviation of +7.4 %. If we assume  $R_{\text{NS}} = 12 \text{ km}$  (13 km) instead, the deviation increases to a value of +15.9 % (+24.4%) above the analytic description. In Table C.1,

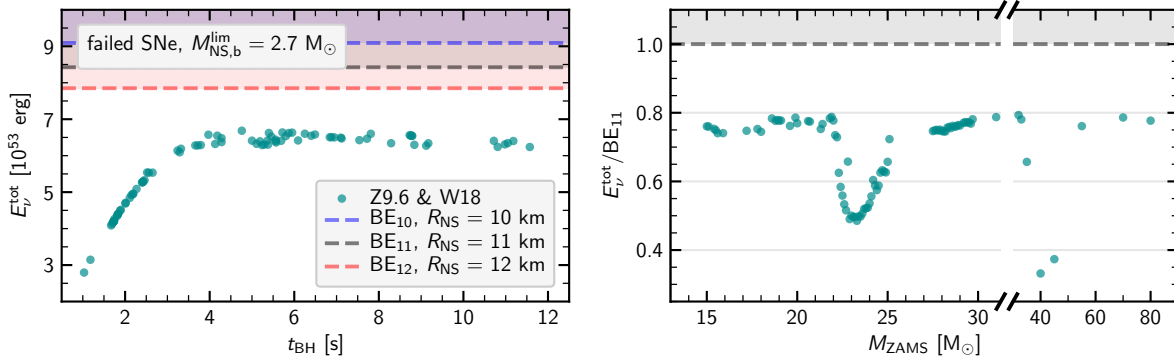


**Figure C.2.:** Comparison of the total neutrino energy,  $E_{\nu}^{\text{tot}}$ , radiated from the failed explosions of our reference set (Z9.6 & W18,  $M_{\text{NS,b}}^{\text{lim}} = 2.7 M_{\odot}$ ) with the maximally available budget of gravitational binding energy (BE) as per an analytic description by Lattimer & Prakash (2001). In the left panel, the relation of  $E_{\nu}^{\text{tot}}$  and the time until BH formation is shown (turquoise dots). The three dashed lines (in blue, black, and red) indicate the PNS’s binding energy at signal termination, computed according to Equation (C.1) with an assumed radius of 10 km, 11 km, and 12 km, respectively. In the right panel, the fraction of the radiated over the maximally available energy is plotted versus ZAMS mass for an assumed PNS radius of 11 km. Note the scale break at  $M_{\text{ZAMS}} \sim 30 M_{\odot}$ .

**Table C.2.:** Maximally available gravitational binding energies as per Equation (C.1) for the different critical baryonic masses  $M_{\text{NS,b}}^{\text{lim}}$  and a PNS radius of 10 km, 11 km, 12 km, and 13 km, respectively. In parentheses, the ratio  $E_{\nu}^{\text{tot}}/\text{BE}$  (largest value out of all calibration sets) is shown.

$M_{\text{NS,b}}^{\text{lim}}$ [ $M_{\odot}$ ]	BE <sub>10</sub> [ $10^{53}$ erg]	BE <sub>11</sub> [ $10^{53}$ erg]	BE <sub>12</sub> [ $10^{53}$ erg]	BE <sub>13</sub> [ $10^{53}$ erg]
2.3	6.8 (77.8 %)	6.3 (84.1 %)	5.9 (90.5 %)	5.5 (96.8 %)
2.7	9.1 (77.3 %)	8.4 (83.4 %)	7.8 (89.5 %)	7.3 (95.6 %)
3.1	11.6 (76.0 %)	10.8 (81.8 %)	10.1 (87.6 %)	9.4 (93.5 %)
3.5	14.4 (74.2 %)	13.4 (79.7 %)	12.5 (85.3 %)	11.8 (90.8 %)
all simulations	<78 %	<85 %	<91 %	<97 %

we show the IMF-weighted mean deviations for all of our calibration models.

Compared to successful explosions, the energy reservoir of BH-forming, failed SNe is generally higher due to the continued gravitational energy release from the infalling mass shells (see Table C.2). However, the binding energy of a maximum-mass PNS solely marks an upper limit for the radiated neutrino energy  $E_{\nu}^{\text{tot}}$ , as an early BH formation can terminate the emission before the energy budget is depleted. This can be seen in the left panel of Figure C.2, where we plot  $E_{\nu}^{\text{tot}}$  for the failed SNe of our reference set (Z9.6 & W18,  $M_{\text{NS,b}}^{\text{lim}} = 2.7 M_{\odot}$ ) against the time until BH formation (turquoise dots). Only the slowly-accreting cases (with  $t_{\text{BH}} \gtrsim 3$  s) come close to the maximally available binding energy according to Equation (C.1), which is indicated by a blue, black, and red dashed line for the radii 10 km, 11 km, and 12 km, respectively. In the right panel, we show the fraction of the radiated over the maximally available energy for an assumed PNS radius of 11 km over the ZAMS mass range of the corresponding progenitors.<sup>16</sup>

In all of our simulations, the neutrino emission from failed SNe lies well within the analytically computed energy budget. For our reference set shown in Figure C.2, at most 80 % of BE<sub>11</sub> are radiated before a BH forms, while the progenitors at around 23 – 24 $M_{\odot}$  and 40 $M_{\odot}$ , which exhibit high mass-accretion rates (see footnote 4 and upper panel of Figure 2.2), feature considerably lower percentages. The outcome of our other calibration sets is very similar (since the emission from failed SNe is dominated by the progenitor-dependent accretion component rather than by the core model). For larger PNS radii applied in Equation (C.1), the ratio  $E_{\nu}^{\text{tot}}/\text{BE}$  is approaching unity, as can be seen in Table C.2 (values in parentheses).

<sup>16</sup>In Appendix A, we pointed out that, at late times, the neutrino luminosities from failed explosions are best described by a pure accretion component with an efficiency parameter  $\eta = 0.51$ . Even if this value is in rough agreement with previous results (Fischer et al., 2009; Hüdepohl, 2014; Müller & Janka, 2014), it should still be deemed uncertain. A higher value of  $\eta$  would enhance the fraction  $E_{\nu}^{\text{tot}}/\text{BE}$ .



# Appendix D.

## Spectral Shapes

Our simplified approach does not provide information on the spectral shape of the neutrino emission. As described in Chapter 3, we hence assume a constant shape parameter  $\alpha$  over the entire length of each signal, which we vary subsequently in Chapter 4. Here, we examine how well our time-integrated spectra match the outcome of more sophisticated simulations with time-dependent  $\alpha$ . Moreover, the range of instantaneous shape parameters used in our study shall be motivated in this context.

In Figure D.1, we compare the normalized time-integrated spectra,  $(dN/dE)/N$ , of electron antineutrinos, obtained from exemplary simulations of our Z9.6 & W18 set for different values of  $\alpha$  (between 2 and 4), with the spectra of six reference models, simulated with the 1D-version of PROMETHEUS-VERTEX (cf. Appendix B). For successful SNe (two upper, and lower left panels), we take models within the same ZAMS mass domain as the respective VERTEX simulations, and such that NSs of roughly comparable baryonic mass  $M_{\text{NS,b}}$  are obtained (see Table D.1). In the lower right panel, we show the spectra of two exemplary failed explosions (s22.1 and s27.9) for a baryonic mass cutoff at  $M_{\text{NS,b}}^{\text{lim}} = 2.7 M_{\odot}$ , compared to the VERTEX models s40s7b2c and s40.0c. These progenitors exhibit different core compactness ( $\xi_{2.5} = 0.59$  (0.26) for s40s7b2c (s40.0c) and  $\xi_{2.5} = 0.31$  (0.23) for s22.1 (s27.9); see footnote 4) and consequently need more or less time to accrete the critical mass for BH formation (however, note the different final PNS masses before BH collapse; see Table D.1).

Our time-integrated spectra (of both successful and failed SNe) show good overall agreement with the VERTEX models if we assume an instantaneous shape parameter  $\alpha$  in the range 2–4. In our DSNB parameter study in Chapter 4, we thus vary  $\alpha$  within this scope. Even if the neutrino spectra slightly deviate from Equation (3.3) after time-integration, we still use the  $\alpha$ -parameter, as defined by Keil et al. (2003), to further quantify the shapes of  $dN/dE$ :

$$\alpha = \frac{2\langle E \rangle^2 - \langle E^2 \rangle}{\langle E^2 \rangle - \langle E \rangle^2} \quad , \quad (\text{D.1})$$

$$\langle E \rangle = \frac{\int dE E (dN/dE)}{\int dE (dN/dE)} \quad , \quad (\text{D.2})$$

$$\langle E^2 \rangle = \frac{\int dE E^2 (dN/dE)}{\int dE (dN/dE)} \quad . \quad (\text{D.3})$$

The values of  $\alpha$  which we obtain for the time-integrated spectra of Figure D.1 are listed in Table D.1 (with the corresponding instantaneous shape parameters given in parentheses). We find that our models match the VERTEX simulations best if we take  $\alpha \approx 3.2$  at every instant of emission for successful SNe in the low-mass range ( $M_{\text{NS,b}} \leq 1.6 M_{\odot}$ ) and  $\alpha \approx 2.7$  for SNe with  $M_{\text{NS,b}} > 1.6 M_{\odot}$  as well as for failed explosions. This choice of values constitutes our reference case in Chapters 4 and 5.

## Appendix D. Spectral Shapes

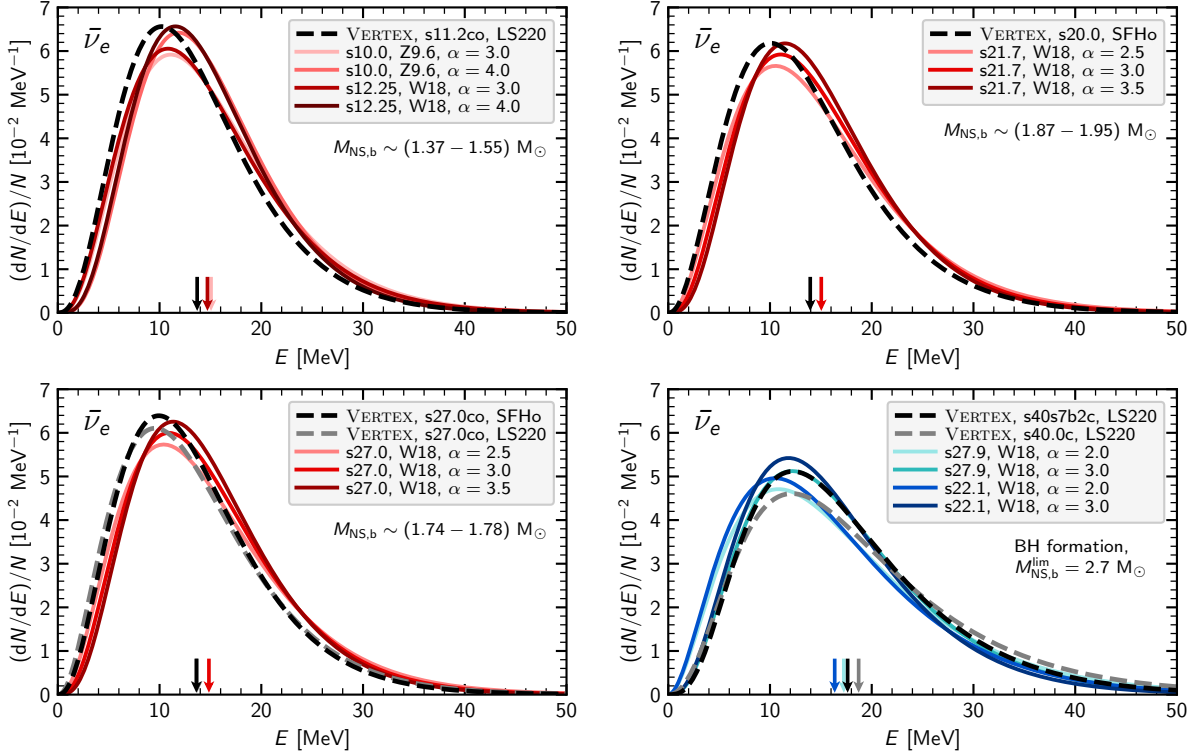


**Figure D.1.:** Normalized time-integrated spectra,  $(dN/dE)/N$ , of electron antineutrinos, obtained from exemplary simulations of our Z9.6 & W18 set, compared to six reference models, simulated with the 1D-version of PROMETHEUS-VERTEX (see Table D.1). In the upper panels and the lower left panel, the spectra of four exploding progenitors (s10.0, s12.25, s21.7, and s27.0) are plotted as solid lines for different values of the instantaneous shape parameter  $\alpha$ ; lighter (darker) colors mark lower (higher) values. The dashed lines indicate the corresponding VERTEX models which lie in the same ZAMS mass domain and yield NSs of comparable baryonic mass  $M_{\text{NS,b}}$ . The lower right panel shows the spectra of two failed explosions (s27.9 and s22.1) with a baryonic mass cutoff at  $2.7 M_{\odot}$ , compared with the VERTEX simulations s40s7b2c and s40.0c, which form BHs at a critical baryonic PNS mass of  $\sim 2.3 M_{\odot}$  after 0.57 s and 2.11 s, respectively. Arrows at the bottom of each panel mark the mean energies  $\langle E \rangle$  of the spectra (cf. Equation (D.2)), as also given in Table D.1.

The mean energies  $\langle E \rangle$  of our time-integrated spectra (second column of Table D.1; also see Figure 2.2), which are indicated by arrows at the bottom of each panel in Figure D.1, agree with the VERTEX models within a few MeV. Our successful SNe, which feature mean energies around  $\sim 15$  MeV rather uniformly over the entire ZAMS mass range, exceed the values obtained with VERTEX by  $\sim 1$  MeV, whereas the two BH-forming models shown in Figure D.1 do not reach as high mean energies as s40s7b2c and s40.0c. The outcome of failed SNe, however, depends strongly on the progenitor structure (which determines the mass accretion) and the mass limit for BH formation, as was discussed in Section 2.3. In Figure D.2 we hence show the normalized time-integrated spectra  $(dN/dE)/N$  additionally for different BH threshold masses (left panel) and progenitors spanning the range from fast to slow mass-accretion (right panel). It is evident that for our BH cases,  $\alpha = 2.7$  yields a good agreement with the VERTEX models, provided the mean energies are similar. For instance, the relatively slow-accreting s27.9 progenitor matches

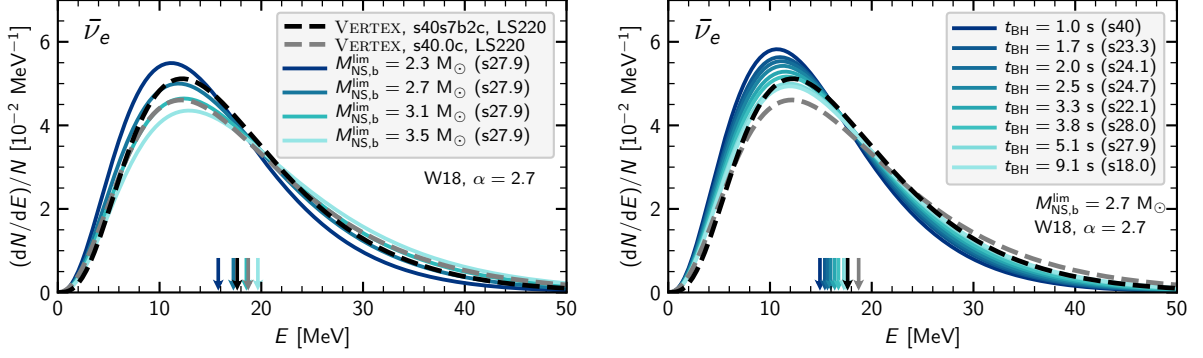


**Figure D.2.:** Normalized time-integrated spectra,  $(dN/dE)/N$ , of electron antineutrinos, obtained from exemplary failed-SN simulations (W18 calibration) with an instantaneous shape parameter  $\alpha = 2.7$  (solid lines), compared to the two models s40s7b2c and s40.0c (black and gray dashed lines), simulated with the 1D-version of PROMETHEUS-VERTEX (cf. lower right panel of Figure D.1). In the left panel, the spectra of the s27.9 progenitor are plotted for different baryonic mass cutoffs  $M_{\text{NS,b}}^{\text{lim}}$  (from  $2.3 M_{\odot}$  in dark to  $3.5 M_{\odot}$  in light blue). The right panel shows the spectra of eight different progenitors with increasing time until BH formation (from 1.0 s in dark to 9.1 s in light blue), for  $M_{\text{NS,b}}^{\text{lim}} = 2.7 M_{\odot}$ . Arrows at the bottom of each panel mark the mean energies  $\langle E \rangle$  of the spectra (cf. Equation (D.2)).

s40s7b2c (s40.0c) with high accuracy for  $M_{\text{NS,b}}^{\text{lim}} = 2.7 M_{\odot}$  ( $3.1 M_{\odot}$ )<sup>17</sup>. Moreover, it can be seen that a later BH formation consistently leads to higher mean energies for both our and the VERTEX simulations. The diversity among the spectra illustrates the need for a large set of long-time BH simulations to properly sample the outcome of the failed channel.

<sup>17</sup>Increasing  $M_{\text{NS,b}}^{\text{lim}}$  by  $0.4 M_{\odot}$  leads to an increase of  $\langle E \rangle$  by  $\sim (1.1 - 1.5) \text{ MeV}$  and, while keeping the instantaneous  $\alpha$  constant, to a decrease of  $\alpha$  of the time-integrated spectra by  $\sim (0.1 - 0.2)$  in case of the s27.9 progenitor.

**Table D.1.:** Mean energies and shape parameters of the time-integrated spectra of electron antineutrinos shown in Figure D.1, according to Equations (D.1)-(D.3). Corresponding values of the instantaneous shape parameters are given in parentheses. The baryonic NS masses of successfully-exploding models are listed in the last column. For failed explosions, the time until BH formation is shown (second to last column), as well as the final baryonic PNS mass before BH collapse (last column).

Model	$\langle E \rangle$ [MeV]	$\alpha$	Compact Remnant	$M_{\text{NS,b}}$ [ $M_{\odot}$ ]
VERTEX, s11.2co, LS220	13.70	2.90	NS	1.366
s10.0, Z9.6	15.06	2.85 (3.0), 3.32 (3.5), 3.78 (4.0)	NS	1.430
s12.25, W18	14.71	2.83 (3.0), 3.29 (3.5), 3.75 (4.0)	NS	1.551
VERTEX, s20.0, SFHo	13.96	2.48	NS	1.947
s21.7, W18	15.04	2.36 (2.5), 2.82 (3.0), 3.28 (3.5)	NS	1.870
VERTEX, s27.0co, SFHo	13.61	2.61	NS	1.772
VERTEX, s27.0co, LS220	13.68	2.25	NS	1.776
s27.0, W18	14.85	2.36 (2.5), 2.83 (3.0), 3.28 (3.5)	NS	1.742
VERTEX, s40s7b2c, LS220	17.63	2.53	BH (0.57 s)	(2.320)
VERTEX, s40.0c, LS220	18.69	1.99	BH (2.11 s)	(2.279)
s22.1, W18	16.36	1.81 (2.0), 2.24 (2.5), 2.67 (3.0)	BH (3.32 s)	(2.7)
s27.9, W18	17.25	1.71 (2.0), 2.11 (2.5), 2.49 (3.0)	BH (5.11 s)	(2.7)

# Appendix E.

## List of Abbreviations

1D	spherically symmetric
2D	axisymmetric
3D	three-dimensional
$\Lambda$ CDM	standard cosmological model with cold dark matter (CDM) and a cosmological constant ( $\Lambda$ )
AIC	accretion-induced collapse
BE	gravitational binding energy
BH(s)	black hole(s)
DSNB	diffuse supernova neutrino background
ECSN(e)	electron-capture supernova(e)
EoS(s)	equation(s) of state
IH	inverted hierarchy (of neutrino masses)
IMF	initial mass function
LM	low-mass
LS180(220)	high-density EoS by Lattimer & Swesty (1991) with incompressibility $K = 180$ MeV ( $K = 220$ MeV)
LSST	Large Synoptic Survey Telescope (Tyson, 2002)
MIC	merger-induced collapse
MSW	Mikheyev-Smirnov-Wolfenstein (Wolfenstein, 1978; Mikheyev & Smirnov, 1985)
NH	normal hierarchy (of neutrino masses)
NS(s)	neutron star(s)
ONeMg	oxygen-neon-magnesium
PNS(s)	proto-neutron star(s)
SFH	star formation history
SFHo	high-density EoS by Steiner et al. (2013)
SK	Super-Kamiokande
SN(e)	supernova(e)
SW14	Sukhbold & Woosley (2014)
WD(s)	white dwarf(s)
WH07	Woosley & Heger (2007)
WH15	Woosley & Heger (2015)
ZAMS	zero-age main sequence



# Software

- PROMETHEUS-HOTB (Janka & Mueller, 1996; Kifonidis et al., 2003; Scheck et al., 2006; Ertl et al., 2016)
- NumPy and Scipy (Oliphant, 2007)
- IPython (Perez & Granger, 2007)
- Matplotlib (Hunter, 2007)



# Bibliography

- Abadie, J., Abbott, B. P., Abbott, R., et al. 2010, *Classical and Quantum Gravity*, 27, 173001
- Abbasi, R., Abdou, Y., Abu-Zayyad, T., et al. 2011, *A&A*, 535, A109
- Abbott, B. P., Abbott, R., Abbott, T. D., et al. 2017, *Physical Review Letters*, 119, 161101
- Abbott, B. P., Abbott, R., Abbott, T. D., et al. 2017, *ApJ*, 848, L12
- Adams, S. M., Kochanek, C. S., Gerke, J. R., Stanek, K. Z., & Dai, X. 2017, *MNRAS*, 468, 4968
- Agafonova, N. Y., Aglietta, M., Antonioli, P., et al. 2015, *ApJ*, 802, 47
- Alexeyev, E. N., Alexeyeva, L. N., Krivosheina, I. V., & Volchenko, V. I. 1988, *Physics Letters B*, 205, 209
- Alsing, J., Silva, H. O., & Berti, E. 2018, *MNRAS*, 478, 1377
- An, F., An, G., An, Q., et al. 2016, *Journal of Physics G Nuclear Physics*, 43, 030401
- Ando, S. 2004, *ApJ*, 607, 20
- Ando, S., & Sato, K. 2003, *Physics Letters B*, 559, 113
- Ando, S., & Sato, K. 2004, *New Journal of Physics*, 6, 170
- Antoniadis, J., Freire, P. C. C., Wex, N., et al. 2013, *Science*, 340, 448
- Arcones, A., Janka, H.-T., & Scheck, L. 2007, *A&A*, 467, 1227
- Arnett, W. D., Bahcall, J. N., Kirshner, R. P., & Woosley, S. E. 1989, *ARA&A*, 27, 629
- Aseev, V. N., Belesev, A. I., Berlev, A. I., et al. 2011, *Phys. Rev. D*, 84, 112003
- Bailyn, C. D., & Grindlay, J. E. 1990, *ApJ*, 353, 159
- Baldry, I. K., & Glazebrook, K. 2003, *ApJ*, 593, 258
- Barranco, J., Bernal, A., & Delepine, D. 2018, *Journal of Physics G Nuclear Physics*, 45, 055201
- Bauswein, A., Just, O., Janka, H.-T., & Stergioulas, N. 2017, *ApJ*, 850, L34
- Bays, K., Iida, T., Abe, K., et al. 2012, *Phys. Rev. D*, 85, 052007
- Beacom, J. F. 2010, *Annual Review of Nuclear and Particle Science*, 60, 439
- Beacom, J. F., & Vagins, M. R. 2004, *Physical Review Letters*, 93, 171101
- Bionta, R. M., Blewitt, G., Bratton, C. B., et al. 1987, *Physical Review Letters*, 58, 1494

## *Bibliography*

- Bisnovatyi-Kogan, G. S., & Seidov, Z. F. 1982, *Soviet Ast.*, 26, 132
- Bollig, R., Janka, H.-T., Lohs, A., et al. 2017, *Physical Review Letters*, 119, 242702
- Bouchet, P., Phillips, M. M., Suntzeff, N. B., et al. 1991, *A&A*, 245, 490
- Brown, J. M., & Woosley, S. E. 2013, *ApJ*, 769, 99
- Buras, R., Rampp, M., Janka, H.-T., & Kifonidis, K. 2006, *A&A*, 447, 1049
- Burrows, A. 1988, *ApJ*, 334, 891
- Burrows, A. 2013, *Reviews of Modern Physics*, 85, 245
- Chakraborty, S., Choubey, S., & Kar, K. 2011, *Physics Letters B*, 702, 209
- Chakraborty, S., Hansen, R., Izaguirre, I., & Raffelt, G. 2016, *Nuclear Physics B*, 908, 366
- Demorest, P. B., Pennucci, T., Ransom, S. M., Roberts, M. S. E., & Hessels, J. W. T. 2010, *Nature*, 467, 1081
- Dewi, J. D. M., Pols, O. R., Savonije, G. J., & van den Heuvel, E. P. J. 2002, *MNRAS*, 331, 1027
- Diehl, R., Halloin, H., Kretschmer, K., et al. 2006, *Nature*, 439, 45
- Doherty, C. L., Gil-Pons, P., Siess, L., Lattanzio, J. C., & Lau, H. H. B. 2015, *MNRAS*, 446, 2599
- Duan, H., Fuller, G. M., & Qian, Y.-Z. 2010, *Annual Review of Nuclear and Particle Science*, 60, 569
- Ebinger, K., Curtis, S., Fröhlich, C., et al. 2018, [arXiv:1804.03182](https://arxiv.org/abs/1804.03182)
- Ertl, T., Janka, H.-T., Woosley, S. E., Sukhbold, T., & Ugliano, M. 2016, *ApJ*, 818, 124
- Farzan, Y., & Palomares-Ruiz, S. 2014, *J. Cosmology Astropart. Phys.*, 6, 014
- Fischer, T., Whitehouse, S. C., Mezzacappa, A., Thielemann, F.-K., & Liebendörfer, M. 2009, *A&A*, 499, 1
- Fischer, T., Whitehouse, S. C., Mezzacappa, A., Thielemann, F.-K., & Liebendörfer, M. 2010, *A&A*, 517, A80
- Graur, O., Poznanski, D., Maoz, D., et al. 2011, *MNRAS*, 417, 916
- Hartmann, D. H., & Woosley, S. E. 1997, *Astroparticle Physics*, 7, 137
- Heger, A., Fryer, C. L., Woosley, S. E., Langer, N., & Hartmann, D. H. 2003, *ApJ*, 591, 288
- Hidaka, J., Kajino, T., & Mathews, G. J. 2016, *ApJ*, 827, 85
- Hirata, K., Kajita, T., Koshiya, M., et al. 1987, *Physical Review Letters*, 58, 1490
- Hopkins, A. M., & Beacom, J. F. 2006, *ApJ*, 651, 142

- Horiuchi, S., Beacom, J. F., & Dwek, E. 2009, *Phys. Rev. D*, 79, 083013
- Horiuchi, S., Beacom, J. F., Kochanek, C. S., et al. 2011, *ApJ*, 738, 154
- Horiuchi, S., Nakamura, K., Takiwaki, T., Kotake, K., & Tanaka, M. 2014, *MNRAS*, 445, L99
- Horiuchi, S., Sumiyoshi, K., Nakamura, K., et al. 2018, *MNRAS*, 475, 1363
- Hüdepohl, L. 2014, PhD thesis, Technische Universität München
- Hüdepohl, L., Müller, B., Janka, H.-T., Marek, A., & Raffelt, G. G. 2010, *Physical Review Letters*, 104, 251101
- Hunter, J. D. 2007, *Computing in Science & Engineering*, 9, 90
- Hurley, J. R., Tout, C. A., Wickramasinghe, D. T., Ferrario, L., & Kiel, P. D. 2010, *MNRAS*, 402, 1437
- Ikeda, M., Takeda, A., Fukuda, Y., et al. 2007, *ApJ*, 669, 519
- Ivanova, N., Heinke, C. O., Rasio, F. A., Belczynski, K., & Fregeau, J. M. 2008, *MNRAS*, 386, 553
- Ivanova, N., & Taam, R. E. 2004, *ApJ*, 601, 1058
- Izaguirre, I., Raffelt, G., & Tamborra, I. 2017, *Physical Review Letters*, 118, 021101
- Janka, H.-T. 2012, *Annual Review of Nuclear and Particle Science*, 62, 407
- Janka, H.-T. 2017, *Handbook of Supernovae*, ISBN 978-3-319-21845-8. Springer International Publishing AG, 2017, p. 1575, 1575
- Janka, H.-T., Hanke, F., Hüdepohl, L., et al. 2012, *Progress of Theoretical and Experimental Physics*, 2012, 01A309
- Janka, H.-T., Müller, B., Kitaura, F. S., & Buras, R. 2008, *A&A*, 485, 199
- Janka, H.-T., & Mueller, E. 1996, *A&A*, 306, 167
- Jeong, Y. S., Palomares-Ruiz, S., Hall Reno, M., & Sarcevic, I. 2018, *J. Cosmology Astropart. Phys.*, 6, 019
- Jones, S., Hirschi, R., Nomoto, K., et al. 2013, *ApJ*, 772, 150
- Jones, S., Röpke, F. K., Pakmor, R., et al. 2016, *A&A*, 593, A72
- Kashyap, R., Haque, T., Lorén-Aguilar, P., García-Berro, E., & Fisher, R. T. 2018, *arXiv:1811.00013*
- Keehn, J. G., & Lunardini, C. 2012, *Phys. Rev. D*, 85, 043011
- Keil, W., & Janka, H.-T. 1995, *A&A*, 296, 145
- Keil, M. T., Raffelt, G. G., & Janka, H.-T. 2003, *ApJ*, 590, 971

## *Bibliography*

- Kennicutt, R. C., Jr. 1998, *ARA&A*, 36, 189
- Kifonidis, K., Plewa, T., Janka, H.-T., & Müller, E. 2003, *A&A*, 408, 621
- Kitaura, F. S., Janka, H.-T., & Hillebrandt, W. 2006, *A&A*, 450, 345
- Kochanek, C. S. 2014, *ApJ*, 785, 28
- Kochanek, C. S., Beacom, J. F., Kistler, M. D., et al. 2008, *ApJ*, 684, 1336-1342
- Kraus, C., Bornschein, B., Bornschein, L., et al. 2005, *European Physical Journal C*, 40, 447
- Krauss, L. M., Glashow, S. L., & Schramm, D. N. 1984, *Nature*, 310, 191
- Lattimer, J. M., & Prakash, M. 2001, *ApJ*, 550, 426
- Lattimer, J. M., & Prakash, M. 2016, *Phys. Rep.*, 621, 127
- Lattimer, J. M., & Swesty, F. D. 1991, *Nuclear Physics A*, 535, 331
- LBNE Collaboration, Adams, C., Adams, D., et al. 2013, arXiv:1307.7335
- Lentz, E. J., Bruenn, S. W., Hix, W. R., et al. 2015, *ApJ*, 807, L31
- Lien, A., Fields, B. D., & Beacom, J. F. 2010, *Phys. Rev. D*, 81, 083001
- Lovegrove, E., & Woosley, S. E. 2013, *ApJ*, 769, 109
- Lunardini, C. 2007, *Phys. Rev. D*, 75, 073022
- Lunardini, C. 2009, *Physical Review Letters*, 102, 231101
- Lunardini, C. 2016, *Astroparticle Physics*, 79, 49
- Lunardini, C., & Peres, O. L. G. 2008, *J. Cosmology Astropart. Phys.*, 8, 033
- Lunardini, C., & Tamborra, I. 2012, *J. Cosmology Astropart. Phys.*, 7, 012
- Malek, M., Morii, M., Fukuda, S., et al. 2003, *Physical Review Letters*, 90, 061101
- Marek, A., Janka, H.-T., & Müller, E. 2009, *A&A*, 496, 475
- Margalit, B., & Metzger, B. D. 2017, *ApJ*, 850, L19
- Mason, B. D., Hartkopf, W. I., Gies, D. R., Henry, T. J., & Helsel, J. W. 2009, *AJ*, 137, 3358
- Mathews, G. J., Hidaka, J., Kajino, T., & Suzuki, J. 2014, *ApJ*, 790, 115
- Melson, T., Janka, H.-T., & Marek, A. 2015, *ApJ*, 801, L24
- Metzger, B. D., Piro, A. L., & Quataert, E. 2009, *MNRAS*, 396, 1659
- Mikheyev, S. P., & Smirnov, A. Y. 1985, *Yadernaya Fizika*, 42, 1441
- Mirizzi, A., Tamborra, I., Janka, H.-T., et al. 2016, *Nuovo Cimento Rivista Serie*, 39, 1

- Miyaji, S., Nomoto, K., Yokoi, K., & Sugimoto, D. 1980, PASJ, 32, 303
- Müller, B. 2016, PASA, 33, e048
- Müller, B., Gay, D. W., Heger, A., Tauris, T. M., & Sim, S. A. 2018, MNRAS, 479, 3675
- Müller, B., Heger, A., Liptai, D., & Cameron, J. B. 2016, MNRAS, 460, 742
- Müller, B., & Janka, H.-T. 2014, ApJ, 788, 82
- Müller, B., Melson, T., Heger, A., & Janka, H.-T. 2017, MNRAS, 472, 491
- Møller, K., Suliga, A. M., Tamborra, I., & Denton, P. B. 2018, J. Cosmology Astropart. Phys., 5, 066
- Nadezhin, D. K. 1980, Ap&SS, 69, 115
- Nakamura, K., Takiwaki, T., Kuroda, T., & Kotake, K. 2015, PASJ, 67, 107
- Nakazato, K. 2013, Phys. Rev. D, 88, 083012
- Nakazato, K., Mochida, E., Niino, Y., & Suzuki, H. 2015, ApJ, 804, 75
- Nicholl, M., Berger, E., Kasen, D., et al. 2017, ApJ, 848, L18
- Nomoto, K. 1984, ApJ, 277, 791
- Nomoto, K. 1987, ApJ, 322, 206
- Nomoto, K., & Kondo, Y. 1991, ApJ, 367, L19
- Nomoto, K., Yamaoka, H., Pols, O. R., et al. 1994, Nature, 371, 227
- O'Connor, E., & Ott, C. D. 2011, ApJ, 730, 70
- Oliphant, T. E. 2007, Computing in Science and Engg., 9, 10
- Ott, C. D., Roberts, L. F., da Silva Schneider, A., et al. 2018, ApJ, 855, L3
- Özel, F., & Freire, P. 2016, ARA&A, 54, 401
- Özel, F., Psaltis, D., Güver, T., et al. 2016, ApJ, 820, 28
- Panter, B., Heavens, A. F., & Jimenez, R. 2003, MNRAS, 343, 1145
- Panter, B., Jimenez, R., Heavens, A. F., & Charlot, S. 2008, MNRAS, 391, 1117
- Pejcha, O., & Thompson, T. A. 2015, ApJ, 801, 90
- Perez, F., & Granger, B. E. 2007, Computing in Science and Engg., 9, 21
- Podsiadlowski, P., Langer, N., Poelarends, A. J. T., et al. 2004, ApJ, 612, 1044
- Poelarends, A. J. T., Herwig, F., Langer, N., & Heger, A. 2008, ApJ, 675, 614
- Priya, A., & Lunardini, C. 2017, J. Cosmology Astropart. Phys., 11, 031

## *Bibliography*

- Radice, D., Burrows, A., Vartanyan, D., Skinner, M. A., & Dolence, J. C. 2017, *ApJ*, 850, 43
- Raithel, C. A., Özel, F., & Psaltis, D. 2018, *ApJ*, 857, L23
- Rampp, M., & Janka, H.-T. 2002, *A&A*, 396, 361
- Reddy, N. A., Steidel, C. C., Pettini, M., et al. 2008, *ApJS*, 175, 48
- Rezzolla, L., Most, E. R., & Weih, L. R. 2018, *ApJ*, 852, L25
- Ruiter, A. J., Ferrario, L., Belczynski, K., et al. 2018, arXiv:1802.02437
- Ruiz, M., Shapiro, S. L., & Tsokaros, A. 2018, *Phys. Rev. D*, 97, 021501
- Rujopakarn, W., Eisenstein, D. J., Rieke, G. H., et al. 2010, *ApJ*, 718, 1171
- Saio, H., & Nomoto, K. 1985, *A&A*, 150, L21
- Sana, H., de Mink, S. E., de Koter, A., et al. 2012, *Science*, 337, 444
- Scheck, L., Kifonidis, K., Janka, H.-T., & Müller, E. 2006, *A&A*, 457, 963
- Schwab, J., Quataert, E., & Kasen, D. 2016, *MNRAS*, 463, 3461
- Shen, H., Toki, H., Oyamatsu, K., & Sumiyoshi, K. 1998, *Nuclear Physics A*, 637, 435
- Shibata, M., Fujibayashi, S., Hotokezaka, K., et al. 2017, *Phys. Rev. D*, 96, 123012
- Smith, N. 2013, *MNRAS*, 434, 102
- Steiner, A. W., Hempel, M., & Fischer, T. 2013, *ApJ*, 774, 17
- Strigari, L. E., Beacom, J. F., Walker, T. P., & Zhang, P. 2005, *J. Cosmology Astropart. Phys.*, 4, 017
- Sukhbold, T., Ertl, T., Woosley, S. E., Brown, J. M., & Janka, H.-T. 2016, *ApJ*, 821, 38
- Sukhbold, T., & Woosley, S. E. 2014, *ApJ*, 783, 10
- Suntzeff, N. B., Phillips, M. M., Elias, J. H., Depoy, D. L., & Walker, A. R. 1992, *ApJ*, 384, L33
- Suwa, Y., Yoshida, T., Shibata, M., Umeda, H., & Takahashi, K. 2015, *MNRAS*, 454, 3073
- Takiwaki, T., Kotake, K., & Suwa, Y. 2014, *ApJ*, 786, 83
- Tamborra, I., Hüdepohl, L., Raffelt, G. G., & Janka, H.-T. 2017, *ApJ*, 839, 132
- Tamborra, I., Müller, B., Hüdepohl, L., Janka, H.-T., & Raffelt, G. 2012, *Phys. Rev. D*, 86, 125031
- Tamborra, I., Raffelt, G., Hanke, F., Janka, H.-T., & Müller, B. 2014, *Phys. Rev. D*, 90, 045032
- Tauris, T. M., Kramer, M., Freire, P. C. C., et al. 2017, *ApJ*, 846, 170
- Tauris, T. M., Langer, N., Moriya, T. J., et al. 2013, *ApJ*, 778, L23

- Tauris, T. M., Langer, N., & Podsiadlowski, P. 2015, *MNRAS*, 451, 2123
- Tominaga, N., Blinnikov, S. I., & Nomoto, K. 2013, *ApJ*, 771, L12
- Tyson, J. A. 2002, *Proc. SPIE*, 4836, 10
- Ugliano, M., Janka, H.-T., Marek, A., & Arcones, A. 2012, *ApJ*, 757, 69
- Utrobin, V. P., Wongwathanarat, A., Janka, H.-T., & Müller, E. 2015, *A&A*, 581, A40
- Walborn, N. R., Lasker, B. M., Laidler, V. G., & Chu, Y.-H. 1987, *ApJ*, 321, L41
- Wanajo, S., Müller, B., Janka, H.-T., & Heger, A. 2018, *ApJ*, 852, 40
- Weaver, T. A., Zimmerman, G. B., & Woosley, S. E. 1978, *ApJ*, 225, 1021
- Wiktorowicz, G., Belczynski, K., & Maccarone, T. 2014, *Binary Systems, their Evolution and Environments*, 37
- Wolfenstein, L. 1978, *Phys. Rev. D*, 17, 2369
- Woosley, S. E., & Heger, A. 2007, *Phys. Rep.*, 442, 269
- Woosley, S. E., & Heger, A. 2015, *ApJ*, 810, 34
- Wu, C.-Y., & Wang, B. 2018, *Research in Astronomy and Astrophysics*, 18, 036
- Yang, H., & Chevalier, R. A. 2015, *ApJ*, 806, 153
- Yüksel, H., Ando, S., & Beacom, J. F. 2006, *Phys. Rev. C*, 74, 015803
- Yüksel, H., & Beacom, J. F. 2007, *Phys. Rev. D*, 76, 083007
- Yüksel, H., & Kistler, M. D. 2015, *Physics Letters B*, 751, 413
- Yüksel, H., Kistler, M. D., Beacom, J. F., & Hopkins, A. M. 2008, *ApJ*, 683, L5
- Zapartas, E., de Mink, S. E., Izzard, R. G., et al. 2017, *A&A*, 601, A29
- Zhang, H., Abe, K., Hayato, Y., et al. 2015, *Astroparticle Physics*, 60, 41



# Danksagung

Allen voran danke ich Thomas Janka für seine sowohl fachlich als auch menschlich durchweg gute Betreuung während der gesamten Zeit meines Master-Projekts, für stets wertvolle und konstruktive Kritik, für seinen Vertrauensvorschuss und dafür, dass er sich immer Zeit genommen hat.

Thomas Ertl danke ich für die Bereitstellung seiner simulierten Neutrinosignale, für Abbildungen 2.1, 2.2 und A.1, für viele anregende Diskussionen, das wiederholte Gegenlesen weiterer Teile der Arbeit und dafür, dass er mir zu Beginn geholfen hat, mich schnell in der Gruppe einzufinden.

Ich danke Robert Glas für seine vielen hilfreichen Tipps rund um Python und Git, für die Bereitstellung seiner LaTeX-Vorlage und insbesondere dafür, dass er ein so guter Bürokollege ist.

Außerdem danke ich Georg Stockinger für sein Update in der Implementierung der Neutrino-Nukleon-Quellterme im Simulationscode PROMETHEUS-HOTB, Robert Bollig für die Bereitstellung seiner VERTEX-Neutrinosignale, sowie allen Mitgliedern unserer Arbeitsgruppe, insbesondere auch denjenigen, die hier nicht explizit genannt wurden, für das durchweg angenehme Arbeitsklima.

Mein besonderer Dank gilt schließlich meiner Familie für die Unterstützung und ihren Rückhalt während meines gesamten Studiums.